



Characteristic limitations of advanced plasticity and hypoplasticity models for cyclic loading of sands

J. Duque¹ · M. Yang² · W. Fuentes³ · D. Mašín¹ · M. Taiebat²

Received: 10 November 2020 / Accepted: 31 October 2021 / Published online: 2 December 2021
© The Author(s), under exclusive licence to Springer-Verlag GmbH Germany, part of Springer Nature 2021

Abstract

Numerous studies in the literature are concerned with proposing new constitutive models for sands to simulate cyclic loading. Despite considerable progress in this area, there are various limitations on their simulation capabilities that are either overlooked or not communicated clearly by the developers. A number of these limitations are rather crucial for the end users, and therefore, providing discussion and analysis of them would be of great value for both applications and future developments. The present work is devoted to discussing seven characteristic limitations, which are frequently observed in cyclic loading simulations. Four advanced constitutive models are considered in this study: two bounding surface elastoplasticity and two hypoplasticity models—with the models in each category following a hierarchical order of complexity. Relevant cyclic loading experimental test data on Toyoura and Karlsruhe fine sands support the analysis. The key issues discussed include stress overshooting, one-way ratcheting in cyclic strain accumulation, liquefaction strength curves, stress attractor in strain-controlled shearing, hypoelasticity, cyclic oedometer stiffness, and effect of drained preloading. The presented results elaborate on the specific limitations and capabilities of these rather advanced models in simulating several essential aspects of cyclic loading of sands.

Keywords Constitutive modelling · Cyclic loading · Elastoplasticity · Hypoplasticity · Sand

1 Introduction

During the last decades, a number of advanced constitutive models have been proposed to simulate the mechanical behavior of sands under cyclic loading, [e.g., 2, 7, 15, 20, 21, 45, 52, 69, 75, 76, 79, 80], just to mention a few. Their capabilities include the consideration of dependency of stiffness and strength on stress and void ratio, incorporation of a Lode angle-dependent critical state surface, reproduction of small strain effects upon loading reversal, and cyclic mobility under undrained cyclic shearing, among many others. Assessment of their capabilities is frequently carried out through direct comparison of their simulation results with a set of routine monotonic

and cyclic experiments, such as undrained and drained cyclic triaxial tests, oedometer tests, cyclic simple shear tests, etc. Although this methodology guarantees some consistent features and cyclic loading response capabilities for the proposed models, their extended validity can be further judged by simulation of some particular paths of more complicated nature. They can be attained by combining the aforementioned routine tests sequentially, such as drained loading followed by undrained loading [10–13], cyclic loading where different principal stress/strain components are simultaneously imposed [24, 31, 34, 40, 53, 55, 58, 60, 72, 77], constant mean effective stress p' paths triaxial tests [49–51, 65], and closed loops at the $q - p'$ space [46, 72]. Under these situations, some particular limitations of models for cyclic loading are repeatedly revealed, for example, overshooting effects, improper accumulation of plastic strains, spoiled dilatancy–contractancy characteristics, or in general, poorly reproduced stiffness. These and other limitations are commonly realized by users. However, they have been less discussed by the model developers.

✉ J. Duque
duquefej@natur.cuni.cz

¹ Charles University, Prague, Czech Republic

² University of British Columbia, Vancouver, Canada

³ Pontificia Universidad Javeriana, Bogotá, Colombia

Different types of constitutive model limitations for simulating cyclic loading are frequently reported in the literature. For example, the overshooting phenomenon has been revealed by some authors and some have proposed solutions for it [e.g., 5, 8, 17, 35, 43, 48]. One-way ratcheting in strain accumulation of undrained cyclic triaxial tests along with cyclic mobility paths has been exhibited by many models [e.g., 7, 19, 22]. Some authors have adopted Lode angle independent critical state which would result in symmetric evolution of shear strain in both directions, that is also not desirable in cyclic triaxial shearing [4, 16, 68]. Excessive plastic accumulation on closed stress loops of small amplitudes, where an elastic behavior is shown by experiments, has been detected by Poblete et al. [46]. Discussion about the lack of plastic deformation obtained under constant stress ratio paths using models with open-wedge yield surfaces can be found elsewhere [e.g., 61, 62]. The recent work by Wichtmann et al. [71] inspected the accuracy of three well-known “advanced” models for cyclic loading, and as a conclusion, a lack of congruence was evidenced on many simulations. Indeed, they also showed that many limitations are shared by the three models, despite the remarked differences in their formulations. All these considerations suggest that models for cyclic loading sharing same limitations are frequently proposed in the literature. In contrast, works oriented to show and discuss these issues from the formulation perspective are scarcely found. This is disappointing, since such a work can serve as a serious warning for future developments and motivate future developers to find key solutions to these characteristic limitations.

The aim of the present paper is to show and discuss some characteristic limitations shared by many constitutive models for cyclic loading of sands. For the purpose of illustration, four constitutive models that have achieved certain success in simulating cyclic loading tests are adopted: the bounding surface plasticity model accounting for fabric change effects on dilatancy upon loading reversal by Dafalias and Manzari [7], hereafter denoted as DM04, the recently proposed model incorporating memory surface and semifluidized state into DM04 by Yang et al. [78], denoted as SANISAND-MSf, the hypoplastic model for sands by Von Wolffersdorf [75] with the Intergranular Strain (IS) extension by Niemunis and Herle [44], henceforth denoted as HP+IS model, and the hypoplastic model for sands extended with Intergranular Strain Anisotropy (ISA) by Fuentes et al. [22], denoted as HP+ISA model. A brief description of their formulations is given in the next section. The present work is not meant to evaluate the accuracy of these models in simulating the experiments, but rather focuses on discussion of the limitations emerging from the lack of constitutive features in their formulations. These carefully selected limitations can pose a challenge to development of new models and meanwhile

provide guidance to improvement on the existing models. To the authors’ knowledge, there still does not exist a constitutive model that can properly tackle all the limitations listed in this paper.

The structure of this paper is organized as follows. At the beginning, a brief description of the constitutive models is provided. Subsequently, the testing materials and model parameters are briefly described. Then, each limitation is expounded by explaining the test, discussing the mechanism, and providing illustrative simulations with the selected models for cyclic loading. At the end, concluding remarks are given. Notation is described in Appendix A.

2 Brief description of models for cyclic loading

Numerical simulations of element tests will be presented in the sequel to illustrate some characteristic limitations of constitutive models for cyclic loading of sands, attributed to certain inadequate considerations or missing ingredients in the mathematical formulations. Two plasticity and two hypoplasticity constitutive models for sand are selected here because they account for various useful features such as stress and void ratio dependency allowing for successful simulations for different stresses and densities and also have achieved certain success in simulation of cyclic response of sands.

The first model is the DM04 proposed by Dafalias and Manzari [7], an extension of a two-surface plasticity model by Manzari and Dafalias [38]. This model is critical state compatible and built in the framework of bounding surface plasticity [6]. It has four conical surfaces in the deviatoric stress space, including a small yield surface centered at the back-stress ratio that obeys kinematic hardening, and three other origin-concentric surfaces: bounding surface, critical state surface, and dilatancy surface. The distances between the current back-stress ratio and its images on bounding and dilatancy surfaces control the plastic modulus and dilatancy, respectively. In addition, the DM04 incorporates a fabric dilatancy tensor to reproduce the cyclic mobility effects observed under undrained cyclic shear tests.

The second model is the SANISAND-MSf proposed by Yang et al. [78]. This model is formulated by introducing two major and two minor modifications into the DM04 model platform with the aim to improve the reference model performance in simulation of undrained cyclic shear tests. The major modifications consist of the incorporation of two new constitutive ingredients, memory surface to well control excess pore pressure generation in pre-liquefaction stage and semifluidized state that allows to capture large shear strain development in post-liquefaction stage. The minor modifications consist of improvement in the

accuracy of the non-associative flow rule in non-proportional loading and the simulation of the cyclic shear stress–strain loops shifting under cyclic triaxial loading. Constitutive relations of the DM04 and SANISAND-MSf models are presented in Table 5, Appendix B.

The third model is the HP+IS, a hypoplasticity sand model proposed by Von Wolffersdorf [75] extended with intergranular strain (IS) according to Niemunis and Herle [44]. The hypoplasticity model without IS extension is characterized by being written through a single tensorial equation, where the stress rate depends directly on the stress, strain rate, and void ratio. Despite its accuracy on the simulation of sands under medium- and large-amplitude cycles ($\|\Delta\epsilon\| > 10^{-3}$) [42, 44, 75], this particular model delivers an excessive plastic accumulation (ratcheting) under cycles of small and medium amplitudes ($\|\Delta\epsilon\| < 10^{-3}$). The intergranular strain (IS) extension proposed by Niemunis and Herle [44] is frequently used to overcome this deficiency and also endows the model with the capabilities in simulations of cyclic tests. This extension incorporates an additional strain-type tensorial variable called the intergranular strain \mathbf{h} to store information about the recent strain history, being properly formulated to increase the stiffness and reduce the plastic accumulation after any event of strain reversal loading. It should be noted that this IS formulation lacks an elastic locus.

The fourth model is the HP+ISA proposed by Fuentes et al. [22]. Similar to the HP+IS model, HP+ISA extends the hypoplasticity model by Von Wolffersdorff [75] by employing the more recently IS formulation proposed originally by Fuentes and Triantafyllidis [20] and enhanced in Fuentes et al. [22]. Important differences compared to the conventional IS formulation by Niemunis and Herle [44] lie in: (a) the evolution of the intergranular strain is now elastoplastic allowing for the incorporation of an elastic locus to the model, (b) the proposed yield surface hardens kinematically, in such fashion, that reproduces a smooth transition between the elastic and plastic behavior, and (c) the formulation accounts for a proper reduction mechanism of the plastic strain rate on sets of identical cycles. Besides these, the mechanism to reproduce cyclic mobility proposed by Fuentes et al. [22] is also adopted. Constitutive relations of the HP+IS and HP+ISA models are provided in Table 6, Appendix B.

3 Description of test materials and model parameters

Two sets of laboratory experimental database on Toyoura and Karlsruhe fine sands, respectively, are considered in this study to analyze the material response under cyclic

loading, in comparison with the corresponding simulations. Toyoura sand has a maximum void ratio $e_{\max} = 0.977$, a minimum void ratio $e_{\min} = 0.597$, a mean diameter $D_{50} = 0.17$ mm and a uniformity coefficient $c_u = 1.7$ [33]. Karlsruhe fine sand (KFS), mainly composed of grains with subangular shape, has a maximum void ratio of $e_{\max} = 1.054$, a minimum void ratio of $e_{\min} = 0.677$, a mean diameter of $D_{50} = 0.14$ mm, and a uniformity coefficient of $c_u = 1.5$ [70]. Tables 1, 2, 3 and 4 present the material parameters for the DM04, SANISAND-MSf, HP+IS and HP+ISA models for Toyoura and Karlsruhe fine sands, respectively. Most of the model parameters are directly taken from the previous works [7, 14, 22, 41, 46, 64, 71, 73, 78] and some of them are tuned a bit to obtain better simulation results. Note that due to different model formulations, parameters with similar physical meaning may have different numerical values in different models. As an example, e_c^{ref} of elastoplastic models differs from e_{c0} of hypoplastic models, although both models predict comparable critical state lines in the space of void ratio versus mean effective stress. This is because the functions defining dependency of critical state void ratio on mean effective stress are different.

4 Analysis of some frequent limitations on models for cyclic loading

The frequent limitations observed on models for cyclic loading are discussed in this section, according to comparisons between laboratory experiments and the corresponding simulations from the selected models.

4.1 Limitation 1: overshooting after reverse loading/immediate reloading paths

In the scenario of reverse loading/immediate reloading, a so-called overshooting phenomenon is observed in many models. Overshooting implies a stress–strain curve which unrealistically overshoots the continuation of a previous curve had the event of reverse loading/immediate reloading not taken place [8]. A simulation example on Karlsruhe fine sand using the HP+IS model is presented in Fig. 1 to illustrate this issue. Initially, an undrained triaxial compression is performed until the vertical strain ϵ_1 reaching 5%, as the reference. Then four additional tests are conducted according to the following procedure: an undrained triaxial compression until $\epsilon_1 = 0.5\%$ followed by a small reverse loading with $\Delta\epsilon_1$ of 0.01%, 0.03%, 0.06%, or 0.09%, respectively, and subsequent reloading until $\epsilon_1 = 5\%$. For all these reverse loading/immediate reloading scenarios, the simulations tend to present a reloading

Table 1 Parameters of the DM04 model for Toyoura sand reported by Dafalias and Manzari [7] and Karlsruhe fine sand modified from Wichtmann et al. [71]

Parameter	Nomenclature	Value Toyoura	Value KFS	Units	Useful test
Elasticity	G_0	125	150	[-]	DMT, UCT
	ν	0.05	0.05	[-]	OED
Critical state	M_c	1.25	1.34	[-]	UMT
	c	0.712	0.7	[-]	UMT
	λ_c	0.019	0.122	[-]	DMT, UMT
	e_c^{ref}	0.934	1.103	[-]	OED
	ξ	0.7	0.205	[-]	DMT, UMT
Yield surface	m	0.01	0.05	[-]	-
Kinematic hardening	h_0	7.05	10.5	[-]	DMT, UCT
	c_h	0.968	0.95	[-]	DMT
	n^b	1.1	1.2	[-]	DMT
Dilatancy	A_0	0.704	0.9	[-]	DMT
	n^d	3.5	2.0	[-]	DMT
Fabric dilatancy	z_{max}	4.0	15.0	[-]	UCT
	c_z	600	2000	[-]	UCT

OED Oedometric test, DMT Drained monotonic triaxial test, UMT Undrained monotonic triaxial test, UCT Undrained cyclic triaxial test

Table 2 Parameters of the SANISAND-MSf model for Toyoura sand and Karlsruhe fine sand

Parameter	Nomenclature	Value Toyoura	Value KFS	Units	Useful test
Elasticity	G_0	125	150	[-]	DMT, UCT
	ν	0.05	0.05	[-]	OED
Critical state	M_c	1.25	1.34	[-]	UMT
	c	0.712	0.7	[-]	UMT
	λ_c	0.019	0.122	[-]	DMT, UMT
	e_c^{ref}	0.934	1.103	[-]	OED
	ξ	0.7	0.205	[-]	DMT, UMT
Yield surface	m	0.01	0.05	[-]	-
Kinematic hardening	h_0	7.05	10.5	[-]	DMT, UCT
	c_h	0.968	0.95	[-]	DMT
	n^b	1.1	1.2	[-]	DMT
Dilatancy	A_0	0.704	0.9	[-]	DMT
	n^d	3.5	2.0	[-]	DMT
	n_g	0.95	0.92	[-]	UCT
Fabric dilatancy	z_{max}	4.0	15.0	[-]	UCT
	c_z	600	2000	[-]	UCT
Memory surface	μ_0	0.5	2.5	[-]	UCT
	u	2.0	1.2	[-]	UCT
Semifluidized state	x	4.3	5.5	[-]	UCT
	c_ℓ	25	30	[-]	UCT

OED Oedometric test, DMT Drained monotonic triaxial test, UMT Undrained monotonic triaxial test, UCT Undrained cyclic triaxial test

stress–strain response well above the reference monotonic curve. The level of the simulated overshooting decreases with the increasing amplitude of reverse loading. However,

for such very small reverse loading/immediate reloading scenarios any overshooting is contradictory to what would be expected from experiments [e.g., 51].

Table 3 Parameters of the HP+IS model for Toyoura sand modified from Ng et al. [41] and Karlsruhe fine sand reported by Wichtmann and Triantafyllidis [73]

Parameter	Nomenclature	Value Toyoura	Value KFS	Units	Useful test
Critical state friction angle	φ_c	30	33.1	[°]	UMT
Granular hardness	h_s	2600	4000	[MPa]	OED
Barotropy exponent	n	0.27	0.27	[-]	OED
Dilatancy exponent	α	0.14	0.14	[-]	DMT
Pyknotropy exponent	β	3.0	2.5	[-]	OED
Minimum void ratio at $p' = 0$	e_{d0}	0.61	0.677	[-]	e_{\min} test
Critical void ratio at $p' = 0$	e_{c0}	0.98	1.054	[-]	e_{\max} test
Maximum void ratio at $p' = 0$	e_{i0}	1.10	1.212	[-]	e_{\max} test
Elastic strain amplitude	R	1×10^{-4}	1×10^{-4}	[-]	UCT
Stiffness factor for reversal loading	m_R	5.5	2.2	[-]	UCT
Stiffness factor for transverse loading	m_T	2.75	1.1	[-]	UCT
Parameter controlling stiffness decay	β_r	0.08	0.1	[-]	UCT
Parameter controlling stiffness decay	χ	1.0	5.5	[-]	UCT

OED Oedometric test, DMT Drained monotonic triaxial test, UMT Undrained monotonic triaxial test, UCT Undrained cyclic triaxial test

Table 4 Parameters of the HP+ISA model for Toyoura sand reported by Poblete et al. [46] and Karlsruhe fine sand modified from Fuentes et al. [22]

Parameter	Nomenclature	Value Toyoura	Value KFS	Units	Useful test
Critical state friction angle	φ_c	30	33.1	[°]	UMT
Granular hardness	h_s	2600	4000	[MPa]	OED
Barotropy exponent	n	0.27	0.27	[-]	OED
Dilatancy exponent	α	0.14	0.14	[-]	DMT
Pyknotropy exponent	β	3.0	2.5	[-]	OED
Minimum void ratio at $p' = 0$	e_{d0}	0.61	0.677	[-]	e_{\min} test
Critical void ratio at $p' = 0$	e_{c0}	0.98	1.054	[-]	e_{\max} test
Maximum void ratio at $p' = 0$	e_{i0}	1.10	1.212	[-]	e_{\max} test
Elastic strain amplitude	R	1×10^{-4}	1×10^{-4}	[-]	UCT
Stiffness factor for reversal loading	m_R	5.0	5.0	[-]	UCT
Minimum IS hardening parameter	β_{h0}	0.3	0.2	[-]	UCT
Maximum IS hardening parameter	β_{hmax}	3.0	3.0	[-]	UCT
Minimum IS exponent	χ_0	5.0	5.0	[-]	UCT
Maximum IS exponent	χ_{max}	18.0	17.7	[-]	UCT
Accumulation rate factor	c_a	0.01	0.018	[-]	UCT
Cyclic mobility factor	c_z	600	300	[-]	UCT

OED Oedometric test, DMT Drained monotonic triaxial test, UMT Undrained monotonic triaxial test, UCT Undrained cyclic triaxial test

To more precisely illustrate this issue, Fig. 2a, b presents two experimental triaxial tests on Toyoura sand from Ishihara [33], including a “monotonic” one and a “cyclic” one. Both experiments were conducted on isotropically consolidated samples with an initial mean stress $p'_0 = 100$ kPa and relative density $D_r = 16\%$. The “monotonic” experiment consists of a drained triaxial compression test ending at a deviatoric stress $q = 80$ kPa

and a subsequent undrained triaxial compression test until reaching a vertical strain $\varepsilon_1 = 20\%$. The “cyclic” experiment follows a similar procedure as the “monotonic” one, and the only difference is that five small undrained reverse loading–reloading cycles are introduced between the drained and undrained loadings. Each cycle follows the sequence: a loading of $\Delta\varepsilon_1 = 0.3\%$, an unloading of $\Delta\varepsilon_1 = 0.03\%$, and a reloading of $\Delta\varepsilon_1 = 0.03\%$. The

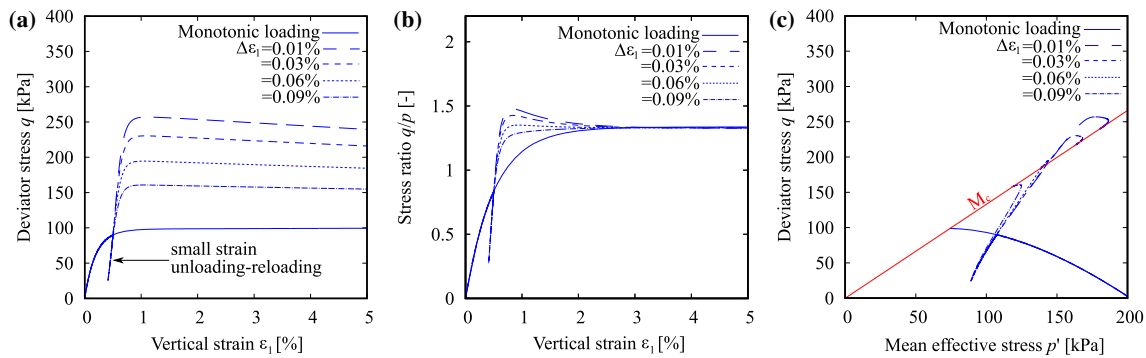


Fig. 1 Simulations with the HP+IS model of an undrained triaxial test with different small strain unloading–reloading cycles on a loose sample ($e_0 = 0.98$) with isotropic consolidation ($p'_0 = 200$ kPa)

experimental path clearly follows the monotonic loading path after the reverse loading/immediate reloading process.

The simulation results of these two experiments using the four selected models are shown in Fig. 2c–j. The simulated stress–strain curve and stress path are quite similar for the DM04 and SANISAND-MSf models, both presenting the overshooting response. This overshooting is caused by the use of a discrete memory variable updated at any stress reversal, which in such small reverse loading/immediate reloading scenarios would lead to an overestimation of the stiffness. Fortunately, the nature of bounding surface plasticity “bounds” the extent of such overshooting to an acceptable level [8].

The simulated stress–strain curve of the HP+IS model in Fig. 2g indicates a significant overprediction of the stiffness after each reloading path, inducing such massive overshooting. This undesired effect can be explained as follows: The IS formulation delivers a sudden increase of stiffness and reduction of the hypoplastic strain rate after each unloading–reloading event, which remains active upon a certain strain amplitude. The size of this amplitude is only controlled by parameters R , β and χ [18, 42]. If the reloading strain amplitude is smaller, an overshooting response is then reproduced by the IS model.

The simulation results of the HP+ISA model in Fig. 2i, j do not indicate the issue of overshooting but the path after each loading cycle stays below the monotonic one, which can be termed as “undershooting”. This is because an elastic threshold strain accounting for memory effects is incorporated in the HP+ISA model, one of the key improvements from HP+IS; however, once the elastic threshold strain is reached, the remaining strain amplitude in which the IS effect is active does not necessarily coincide with the unloading–reloading strain amplitude, which causes the undershooting problem.

To mitigate the overshooting limitation in bounding surface plasticity models, it may be necessary to memorize the recent loading history to adjust the updating of the

related discrete memory variable. Dafalias [6] outlined a way of updating the back-stress ratio at the initiation of a new loading process, and the implementation details were expounded in Dafalias and Taiebat [8]. This overshooting correction scheme can be easily incorporated in the SANISAND-MSf model. The improved simulation results are presented in Fig. 3, illustrating the effectiveness of the scheme. For addressing the overshooting problem in the hypoplastic models, Niemunis [42] suggested using an overlay approach. This idea still requires further investigation. A simpler solution may be coupling the intergranular strain model with the asymptotic state boundary surface (ASBS) of the hypoplastic models in such a way that the ASBS defines the maximum stress states of the model [3]. Such an approach would, however, only correct major overshooting events where stress reaches states outside ASBS. Overshooting inside ASBS, such as the one presented in Fig. 1b, would still be present.

4.2 Limitation 2: shear strain accumulation in cyclic mobility

When medium dense or dense sand elements are subjected to undrained cyclic shearing with a constant shear stress amplitude, the samples present a gradual reduction of mean effective stress p' . Eventually the material undergoes the so-called cyclic mobility, in which the stress path experiences typical butterfly shape with momentary liquefaction state (p' near zero) while the cyclic shear strain amplitude increases cycle by cycle. Large but limited shear strain develops after a sufficient number of loading cycles. The simple shear experiments usually manifest rather symmetric stress–strain loops while the triaxial ones tend to accumulate more strain in the extension side compared with the compression side but still with stress–strain loops expanding on both sides. An undrained cyclic triaxial test of $q^{\text{amp}} = 60$ kPa on Karlsruhe fine sand with initial mean stress $p'_0 = 200$ kPa and $D_r = 67\%$ [73] is presented in

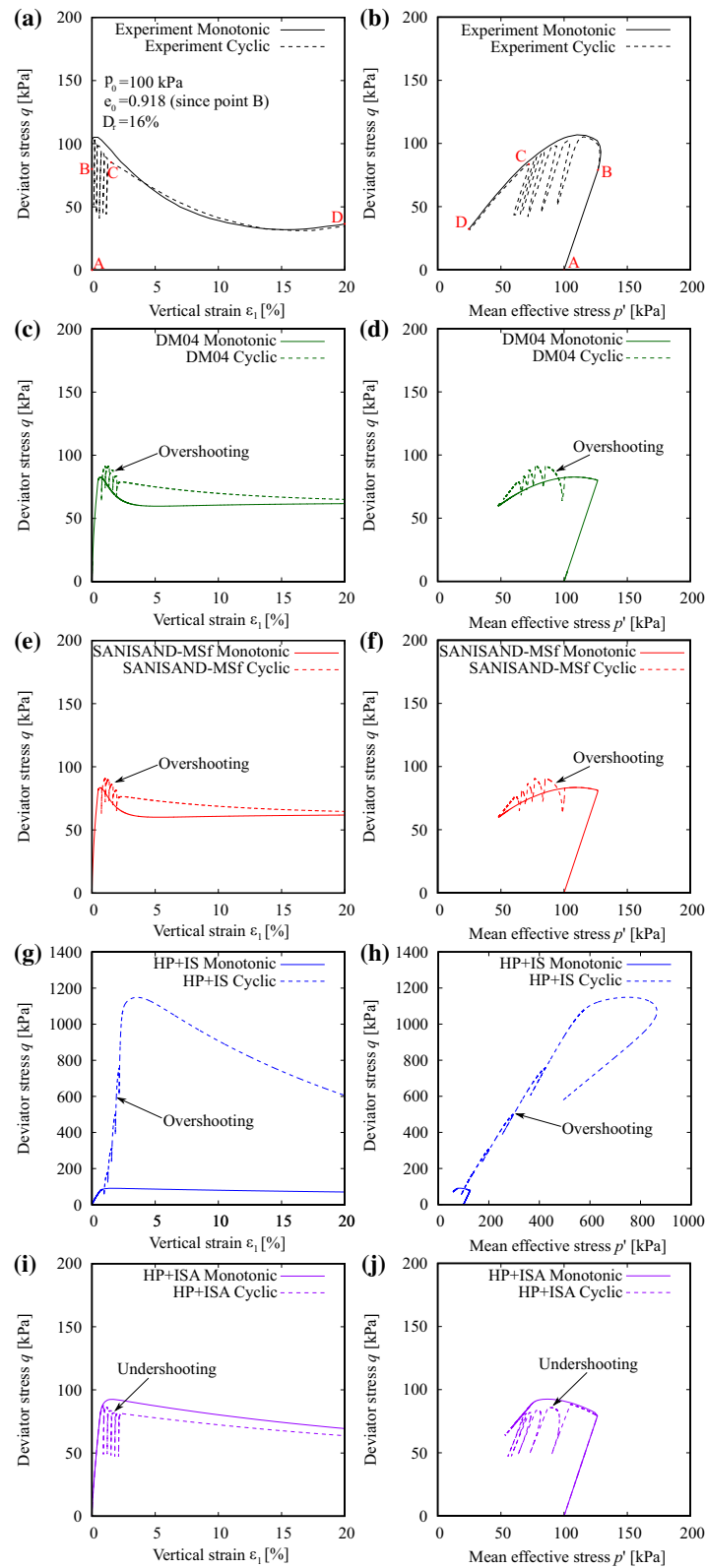


Fig. 2 Monotonic and cyclic triaxial tests on Toyoura sand. Loose sample ($D_r = 16\%$) with isotropic consolidation ($p'_0 = 100$ kPa): (a, b) Experiments reported by Ishihara [33]; and the corresponding simulations using (c, d) DM04; (e, f) SANISAND-MSf; (g, h) HP+IS; (i, j) HP+ISA

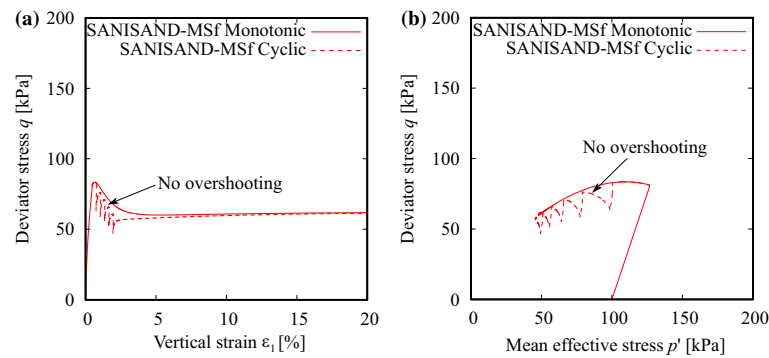


Fig. 3 Simulations of the monotonic and cyclic triaxial tests on Toyoura sand with the SANISAND-MSf model and the overshooting correction proposed by Dafalias and Taiebat [8]

Fig. 4a, b. Clearly one can observe the butterfly shape in Fig. 4a and gradually increasing amplitude of axial strain in subsequent loading cycles in Fig. 4b.

To adequately capture the response in these undrained cyclic triaxial tests, a model should have at least three considerations: (i) elevated contraction in reverse loading following a dilation response, bringing the stress path to a nearly lock-up butterfly shape, (ii) progressive reduction of shear stiffness at the liquefaction state in subsequent cycles, and (iii) modeling the two-way non-symmetric evolution of shear strain, i.e., in both compression and extension directions. The first two considerations have been discussed in a number of constitutive modeling studies [e.g., 16, 28, 2, 80, 37], and the third one has been studied and addressed more recently by Yang et al. [78].

The simulation results of the undrained cyclic triaxial test using DM04, SANISAND-MSf, HP+IS, and HP+ISA models are presented in Fig. 4c–j. Clearly all the models except HP+IS can achieve a satisfying butterfly shape in the stress path, as they account for consideration i mentioned above by incorporating the fabric dilatancy tensor initially proposed by Dafalias and Manzari [7]. However, the simulated stress–strain loops of DM04, HP+IS, and HP+ISA manifest an unrealistic one-way ratcheting, as they do not have mechanisms for the considerations ii and iii mentioned above. The SANISAND-MSf is the only model able to reproduce the increasing double amplitude of cyclic shear strains as it tackles the two aforementioned issues by introducing the following additional constitutive ingredients. The first is significantly reducing the dilatancy and plastic modulus at low mean effective stresses or the so-called semifluidized state, via a novel internal variable called “strain liquefaction factor” (SLF), which evolves only at low mean effective stresses. This mechanism, originally proposed by Barrero et al. [2], is to reproduce shear strain development in the liquefaction state. The second consists of dividing the dilatancy and plastic modulus by a common term with n_g a model parameter as

listed in Table 2, with the goal to balance the relative magnitude of shear strain amplitudes in triaxial compression and extension.

4.3 Limitation 3: cyclic liquefaction strength curves

Cyclic liquefaction failure or initial liquefaction is usually defined as the point at which excess pore pressure ratio approaches 1, or the single or double strain amplitudes reach some limiting values. Cyclic liquefaction of saturated sand can be triggered by different combinations of uniform cyclic stress ratio (CSR), which is the uniform cyclic shear stress divided by initial effective confining stress, and the number of loading cycles [30]. The liquefaction strength curve, i.e., the plot of CSR versus the number of cycles to initial liquefaction N_{ini} , are of practical importance for assessing the success of a sand constitutive model in simulation of cyclic liquefaction.

Under cyclic triaxial conditions, the CSR is defined as the ratio of the deviatoric stress to two times the initial mean effective stress, i.e., $CSR = q^{amp}/(2p'_0)$. In the literature, different criteria were proposed to define initial liquefaction. A common approach is based on the excess pore pressure ratio $r_u = u_w^{acc}/p'_0 = 0.95$ [1, 9, 54] or $r_u = 1$ [29, 70, 73], where u_w^{acc} is the excess pore water pressure. In addition, some other works defined initial liquefaction based on a single strain amplitude (maximum strain in a given cycle only in compression or extension) of $\epsilon_1^{SA} = 2.5\%$ [e.g., 57, 59, 23, 47] or double strain amplitudes (the strain amplitude of a given cycle in compression and extension) of $\epsilon_1^{DA} = 5\%$ [e.g., 27, 32, 66]. While these three criteria preserve consistence of cyclic liquefaction resistance in the experiments, the simulations may present different response due to some deficiencies or missing features in the adopted constitutive models. For example, under undrained cyclic triaxial shearing some models may not reach $r_u = 0.95$ or $\epsilon_1^{DA} = 5\%$ for certain states, but still

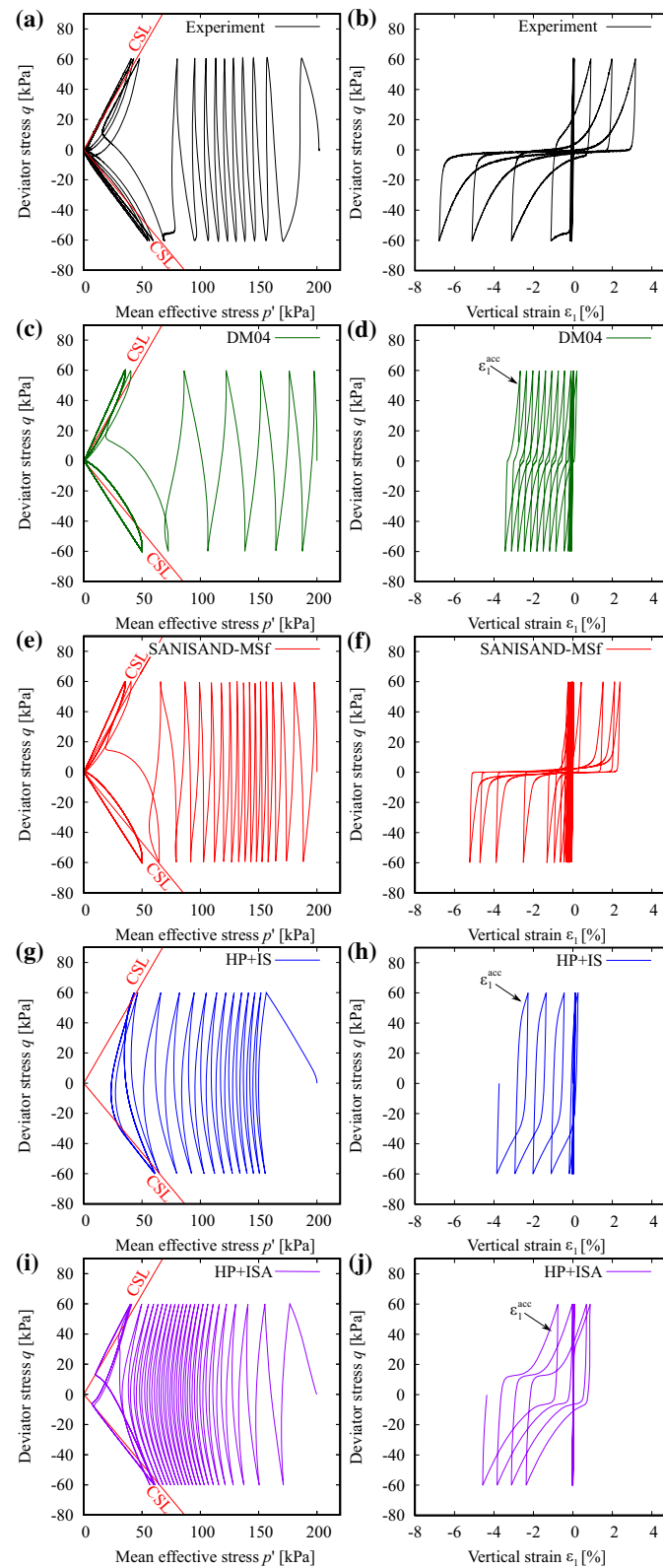


Fig. 4 Undrained cyclic triaxial test on Karlsruhe fine sand. Medium density sample ($D_r = 67\%$) with isotropic consolidation ($p'_0 = 200$ kPa) and stress cycles of $q^{amp} = 60$ kPa: **(a, b)** Experiments reported by Wichtmann and Triantafyllidis [73]; and the corresponding simulations using **(c, d)** DM04; **(e, f)** SANISAND-MSf; **(g, h)** HP+IS; **(i, j)** HP+ISA

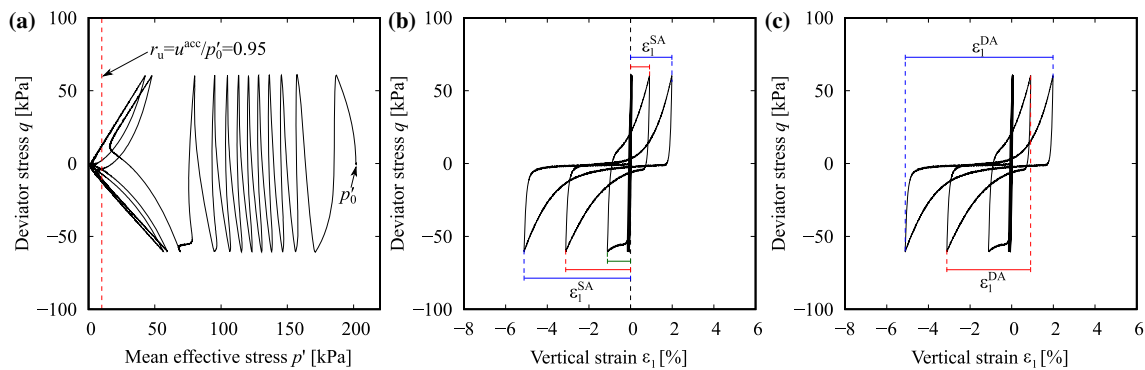


Fig. 5 Schematic illustration of the meanings of excess pore pressure ratio r_u , single strain amplitude ε_1^{SA} , and double strain amplitude ε_1^{DA} in undrained cyclic triaxial shearing, for checking the corresponding selected liquefaction criteria based on $r_u = 0.95$, $\varepsilon_1^{SA} = 2.5\%$, and $\varepsilon_1^{DA} = 5\%$

develop sufficient one-way accumulation of strain to meet $\varepsilon_1^{SA} = 2.5\%$. To give a thorough evaluation of the capabilities of the constitutive models in capturing cyclic liquefaction resistance, three different criteria for initial liquefaction were considered in this paper to generate the $CSR - N_{ini}$ curves: (a) excess pore pressure ratio $r_u = 0.95$, (b) axial strain in single amplitude of $\varepsilon_1^{SA} = 2.5\%$, and (c) axial strain in double amplitude of $\varepsilon_1^{DA} = 5\%$, with the definitions illustrated in Fig. 5.

To adequately simulate the cyclic liquefaction strength curves, in addition to the three consideration mentioned in Sect. 4.2, the model should have a mechanism to control the pace of reduction of effective stress or development of shear strain in various undrained cyclic loading scenarios. Considering that the models can often be calibrated to reasonably reproduce cyclic accumulation at a single loading scenario (but, with the same set of parameters, fail in other loading scenarios), the most straightforward approach to correct the shape of $CSR - N_{ini}$ is to consider state-dependent model parameters. Of course, such a dependency needs to introduce further parameters, which complicates the model formulation and calibration. Adequacy of such a change would thus have to be thoroughly evaluated using experimental data sets on different soils.

To assess the performance of the four constitutive models in the present work in capturing the corresponding liquefaction strength curves, the experimental $CSR - N_{ini}$ curves for Karlsruhe fine sand were constructed using the database of 22 undrained cyclic triaxial tests reported by Wichtmann and Triantafyllidis [73]. Samples were categorized in three range of densities: loose, medium dense, and dense with mean relative densities of 26, 63, and 81%, respectively. The $CSR - N_{ini}$ curves of Karlsruhe sand for all these three criteria are presented in Fig. 6. The corresponding simulations were performed considering the experimental average density of each range, an initial mean effective pressure $p'_0 = 100$ kPa, and a range of CSR. The results presented also in Fig. 6 show a number of

limitations in the simulation capabilities that deserve to be discussed.

In particular, the DM04 simulations show much steeper strength curves than the experiments for the criteria of $r_u = 0.95$ and $\varepsilon_1^{SA} = 2.5\%$ as shown in Fig. 6a, b. This points to a deficiency in the model formulation to control the pace of reduction in effective stress in various levels of CSR. Setting this aside, note that the DM04 simulations do not reach the $\varepsilon_1^{DA} = 5\%$ and so they are absent from Fig. 6c. Recalling the stress–strain plots from the previous section, contrary to the experiments the DM04 shows a one-way ratcheting of strains in the extension direction, but with a locked ε_1^{DA} much smaller than 5%.

The SANISAND-MSf simulations show a significantly improved performance for all three criteria. More specifically, it shows much improved performance in the number of cycles to reach $r_u = 0.95$ as shown in Fig. 6a. This is due to the memory surface mechanism controlling the stiffness in the pre-liquefaction stage. The simulations of SANISAND-MSf also reach the $\varepsilon_1^{DA} = 5\%$ contrary to what was observed in case of DM04, with a reasonable performance as shown in Fig. 6b. This is due to the semifluidized state mechanism controlling the stiffness in the post-liquefaction stage. One still can observe that despite its excellent performance in capturing the cyclic liquefaction curves of loose and medium dense states, the SANISAND-MSf simulations show slightly steeper curves than the experiments for the dense states.

The performance of the HP+IS model is rather poor considering that it cannot reach the criterion $r_u = 0.95$ in any of the three densities, and $\varepsilon_1^{DA} = 5\%$ for medium dense and dense states, due to missing features accounting for the considerations i and ii of Sect. 4.2, respectively. The simulations can reach the $\varepsilon_1^{SA} = 2.5\%$ because this model simulates a non-realistic ratcheting of cyclic shear strain shown in Fig. 4h. However, the simulated curves look steeper than the experiments, implying that the model is

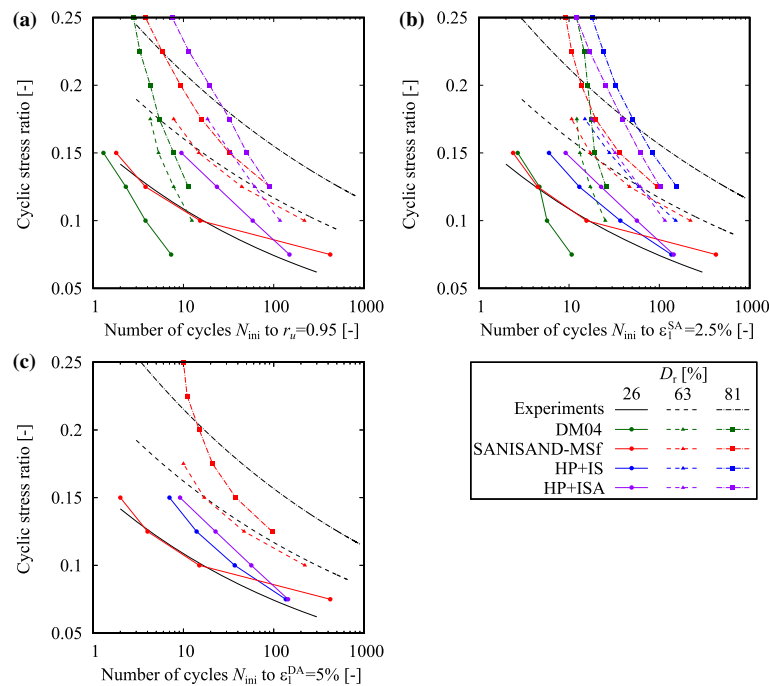


Fig. 6 Liquefaction strength curves of Karlsruhe fine sand at different densities and for different liquefaction criteria: (a) $r_u = 0.95$, (b) $\epsilon_1^{SA} = 2.5\%$ and (c) $\epsilon_1^{DA} = 5\%$

incapable of controlling the pace of shear strain development in various levels of CSR.

In contrast to the HP+IS, the HP+ISA simulations can reach $r_u = 0.95$ due to incorporation of fabric-dilatancy tensor but produce a steeper CSR- N_{ini} curves than the experiments. The HP+ISA model needs improvement to handle the pace of pore pressure generation in various levels of CSR and D_r . The model performance related to the $\epsilon_1^{SA} = 2.5\%$ is very similar to that of the HP+IS, with the same reason explained above. The criterion $\epsilon_1^{DA} = 5\%$ is only reached for the loose state and not the medium dense and dense states. This is because the model cannot simulate large shear strain development sufficiently, related to consideration ii of Sect. 4.2.

4.4 Limitation 4: reaching liquefaction for dense samples under undrained cyclic shearing with constant large strain amplitude

Laboratory experiments of undrained cyclic triaxial tests with constant large strain amplitude $\|\epsilon_1^{amp}\| > 10^{-2}$ on dense sand samples of $D_r > 70\%$ indicate occurrence of liquefaction state after sufficient shearing [36, 39, 67, 70]. According to Gudehus [25], the liquefaction state of $p' = q = 0$ is an attractor of the stress path. In addition, the deviatoric stress amplitude q^{amp} progressively decreases along the cyclic shearing till it vanishes $q^{amp} = 0$ at the liquefaction state. Figure 7a, b presents an experimental

test with $\epsilon_1^{amp} = 1\%$ from Wichtmann and Triantafyllidis [74] imposed on an isotropically consolidated dense sample of Karlsruhe fine sand with initial mean stress $p'_0 = 700$ kPa and relative density $D_r = 101\%$. Along the undrained cyclic shearing, one can observe the gradual degradation of mean effective stress and progressive reduction of q^{amp} . The sample falls into liquefaction state after 57 loading cycles, where $q^{amp} = 0$ and the stiffness vanishes. Note that tests on dense samples have been selected in this section to demonstrate model shortcomings, as predictions are typically more problematic than predictions of equivalent experiments on medium dense and loose samples. To properly capture such behavior, the model should have the capabilities of (i) dragging stress path to liquefaction state upon reverse loading from a considerable dilation period and (ii) liquefaction-induced degradation of stiffness. These required capabilities are same as the first two considerations mentioned in Sect. 4.2.

The simulation results of the experiment using the DM04 model are presented in Fig. 7c, d. The model is able to capture the attractor $p' = q = 0$ despite missing the number of cycles to get there. The latter is partly related to the choices of fabric dilatancy parameters, i.e., c_z and z_{max} in Table 1, which following the dilation response result in significant contraction upon reverse loading. To improve the simulation of the number of cycles to liquefaction in this case, one may consider making the c_z density-dependent. The DM04 simulation results also show that the stress

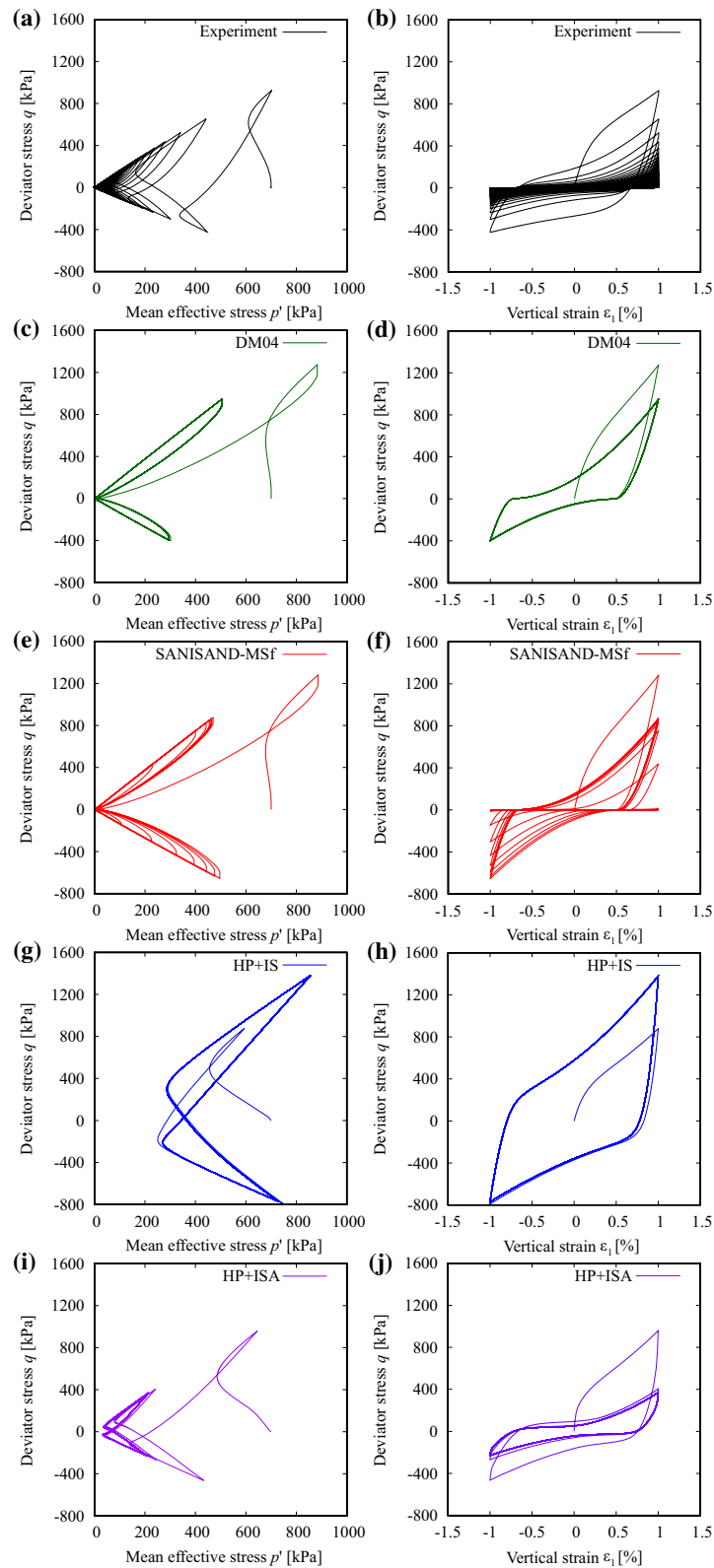


Fig. 7 Undrained cyclic triaxial test on Karlsruhe fine sand. Dense sample ($D_r = 101\%$) with isotropic consolidation ($p'_0 = 700$ kPa) and strain cycles of large amplitude ($\epsilon_1^{\text{amp}} = 1\%$): (a, b) Experiments reported by Wichtmann and Triantafyllidis [74]; and the corresponding simulations using (c, d) DM04; (e, f) SANISAND-MSf; (g, h) HP+IS; (i, j) HP+ISA

path and stress–strain loops get lockup after the first loading cycle and do not replicate the reduction of q^{amp} as shown in the experiment. This is because in the subsequent locked-up stress loops around the liquefaction state, the DM04 does not progressively degrade the plastic modulus. The SANISAND-MSf simulation results are shown in Fig. 7e, f. Here, the model can gradually decrease the plastic modulus at low effective stresses by incorporating the semifluidized state. Therefore, it captures the progressive reduction of q^{amp} and degradation of stress–strain loops to a nearly flat one after several loading cycles, comparable with the experiment.

Simulations with the HP+IS model are presented in Fig. 7g, h and show a serious flaw: The stress path gets locked up before reaching $p' = 0$, and therefore, they do not reach the attractor $p' = q = 0$. As a result, the model also cannot simulate the progressive reduction of q^{amp} . The underlying reasons for these shortcomings are same as those presented earlier for simulation of cyclic mobility. It is worth noting that by incorporating the anisotropic critical state theory to influence the dilation and shear strength, Liao and Yang [37] successfully simulated this type of experiment using a modified version of the HP+IS model. Finally, simulations with HP+ISA model are presented in Fig. 7i, j and show that the model approaches (but not sufficiently) the attractor $p' = q = 0$. Similar to the DM04, this model also does not adequately capture the continued reduction of q^{amp} in subsequent cycles. This is because the model adopts a strain-based version of the fabric dilatancy feature of DM04, to capture the cyclic mobility effect, but does not degrade the stiffness in a progressive fashion.

4.5 Limitation 5: significant plastic accumulation on small $q-p'$ closed loop cycles and artificial accumulation

In addition to the popular one-dimensional cyclic loading type such as cyclic triaxial or simple shear tests, multidimensional cyclic loading generated by varying multiple

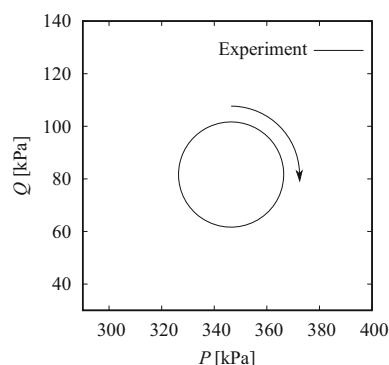


Fig. 8 Cyclic loading path in the $Q - P$ space

components of the stress or strain tensor is also very interesting and meaningful considering the three-dimensional nature of the loading conditions in the field. One such example was performed by Poblete et al. [46] on Karlsruhe fine sand and is illustrated in Fig. 8. The test consists of a multidimensional stress path under triaxial conditions, describing a circle in the space of the invariants $P = \sqrt{3}p'$ and $Q = \sqrt{2/3}q$ (note that $P^2 + Q^2 = \|\boldsymbol{\sigma}\|^2$). To achieve this, Q and P were simultaneously controlled through the following parametric equations:

$$P(t) = 200\sqrt{3} + 20 \sin\left(\frac{2\pi}{200}t\right), \quad (1)$$

$$\text{and } Q(t) = 100\sqrt{\frac{2}{3}} + 20 \sin\left(\frac{2\pi}{200}t + \frac{\pi}{2}\right)$$

or equivalently,

$$\sigma_1 = \frac{800}{3} + \frac{20}{\sqrt{3}} \sin\left(\frac{2\pi}{200}t\right) + \frac{40}{3} \sqrt{\frac{3}{2}} \sin\left(\frac{2\pi}{200}t + \frac{\pi}{2}\right) \quad (2)$$

$$\sigma_2 = \sigma_3 = \frac{500}{3} + \frac{20}{\sqrt{3}} \sin\left(\frac{2\pi}{200}t\right) - \frac{20}{3} \sqrt{\frac{3}{2}} \sin\left(\frac{2\pi}{200}t + \frac{\pi}{2}\right) \quad (3)$$

where t is the time. The corresponding experimental results within 30 loading cycles are given in Fig. 9a–c. One can observe a negligible accumulation of vertical strains ($\varepsilon_1^{\text{acc}} \approx 0$) along the cyclic shearing and the void ratio does not change noticeably either, implying an almost elastic response. It can be used to calibrate model parameters related to elasticity or judge the model performance in handling the plastic modulus during the transition from purely elastic to elastoplastic loading.

We now proceed to provide some simulation results with the aforementioned four constitutive models. The initial conditions of the sample follow $\sigma_1 = 283.0$ kPa, $\sigma_2 = \sigma_3 = 158.5$ kPa and $e_0 = 0.857$. The simulations were performed by controlling the Roscoe stress invariants according to Eq. 1 and are sequentially shown in Fig. 9d–o. Unlike the experiment, all the simulations exhibit significant accumulations of plastic strain and noticeable contraction except the HP+ISA model.

The mismatch between simulations of these three models and the experiment is attributed to the inability to deactivate the plastic strain rate. For DM04 (Fig. 9d–f) and SANISAND-MSf (Fig. 9g–i) models, this inability comes from (a) the rather small size of yield surface (model parameter m in Tables 1 and 2) and (b) the small values of model parameters related to plastic modulus (such as h_0). Had these two been increased by a certain amount, the

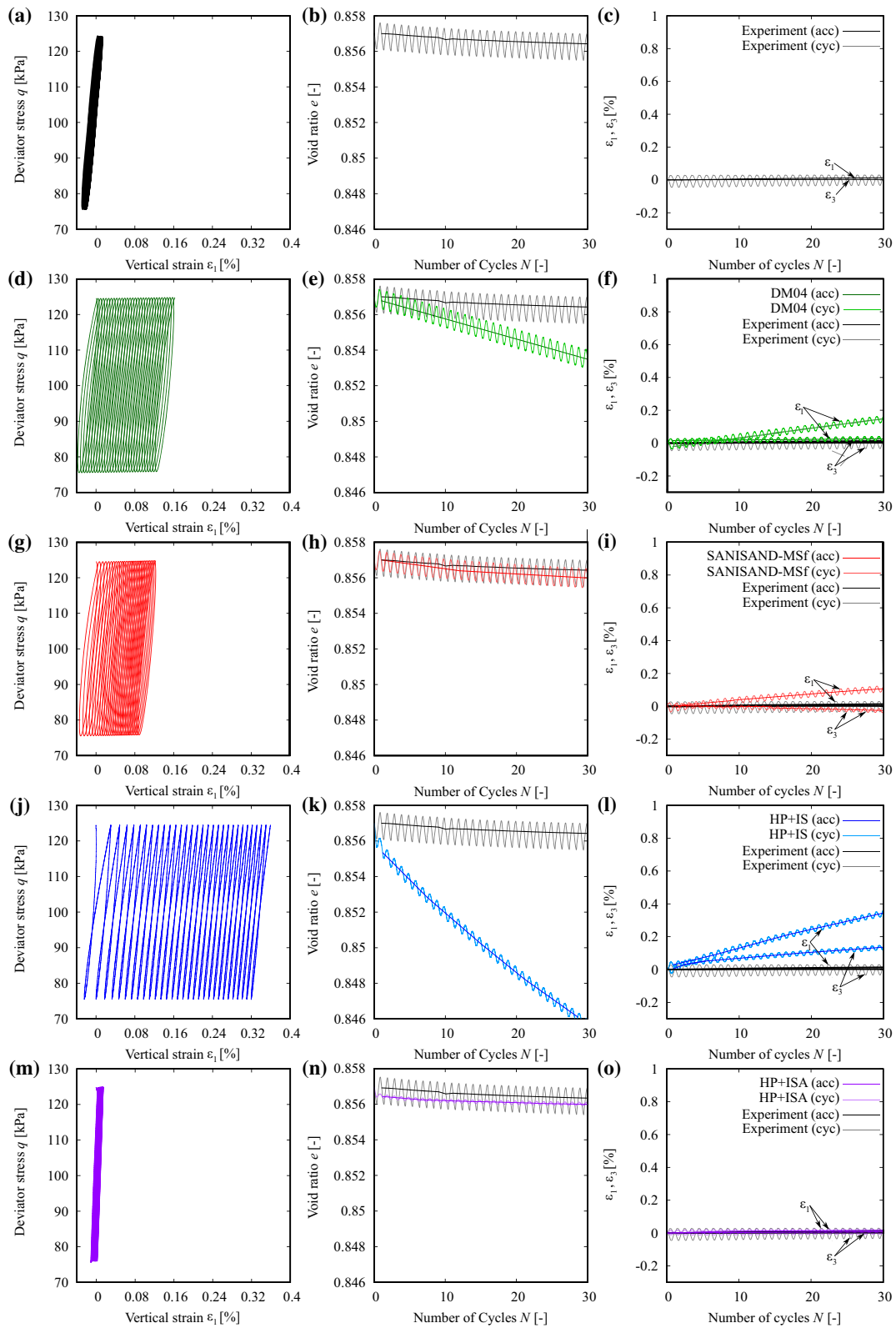


Fig. 9 (a–c) Experiment on Karlsruhe fine sand reported by Poblete et al. [46]; and the corresponding simulations using (d–f) DM04; (g–i) SANISAND-MSF; (j–l) HP+IS; (m–o) HP+ISA

simulations would match the experiment better. An improvement in the SANISAND-MSf simulation compared with DM04 is due to the new constitutive ingredient of memory surface, which stiffens the model when reverse loading occurs. In particular, the simulation of void ratio versus N is very promising and the magnitude of strain components is also reduced a bit. The HP+IS model does not incorporate any elastic locus, but delivers a linear form of the equation when the condition ($\vec{h} : \vec{\epsilon} = -1$) holds for the whole cycle. The latter condition is only possible when performing a very small strain amplitude under one-directional loading conditions. Hence, it is not possible to have such condition on a $q - p'$ loop. The HP+ISA model incorporates a bubble shaped elastic locus within the strain space. From the four selected models, this is the only one able to deactivate completely the plastic strain rate under such path. However, it is still producing very small plastic strain rate, related to the second cause explained in the next paragraph, but remains the most successful in the simulation of this type of loading. These results show us the advantage of using a strain-based yield surface, as in HP+ISA, rather than a stress-based yield surface.

One may doubt the artificial accumulation due to incorporation of hypoelectricity in the models, a quite common feature adopted in sand models. The selection of a hypoelectric stiffness is usually justified by researchers with the argument that the resulting artificial accumulation is almost negligible for most practical problems. However,

Poblete et al. [46] showed that multidimensional stress paths under triaxial conditions in the $q - p'$ space, such as a circle in the $q - p'$ space, provide much more artificial accumulation than unidirectional loading (e.g., conventional undrained cyclic triaxial loading), the latter frequently used to test the performance of models. The accumulation by the hypoelectric tensors is analyzed in Fig. 10 through the simulation of the same experimental test. The plastic component of each model is thereby not considered. Note that the vertical axes of Figs. 9 and 10 are different to observe in detail the effect of the artificial accumulation. The simulation results show an accumulation of strains with all models and a reduction in the void ratio by the hypoelectric-type models. The magnitude of the exhibited accumulation is small but not negligible. In order to address this issue, models may be extended considering hyperelastic stiffness. Comparison of Figs. 9 and 10, however, demonstrates that hypoelectric stiffness is not the major cause of excessive accumulation in closed loop cycles.

4.6 Limitation 6: wrong oedometric stiffness

Oedometric tests are of particular importance for settlement predictions on many engineering problems. When the vertical loading is of cyclic nature and occurs under drained conditions, correct assessment of cyclic models on the reproduction of oedometric cycles is of crucial

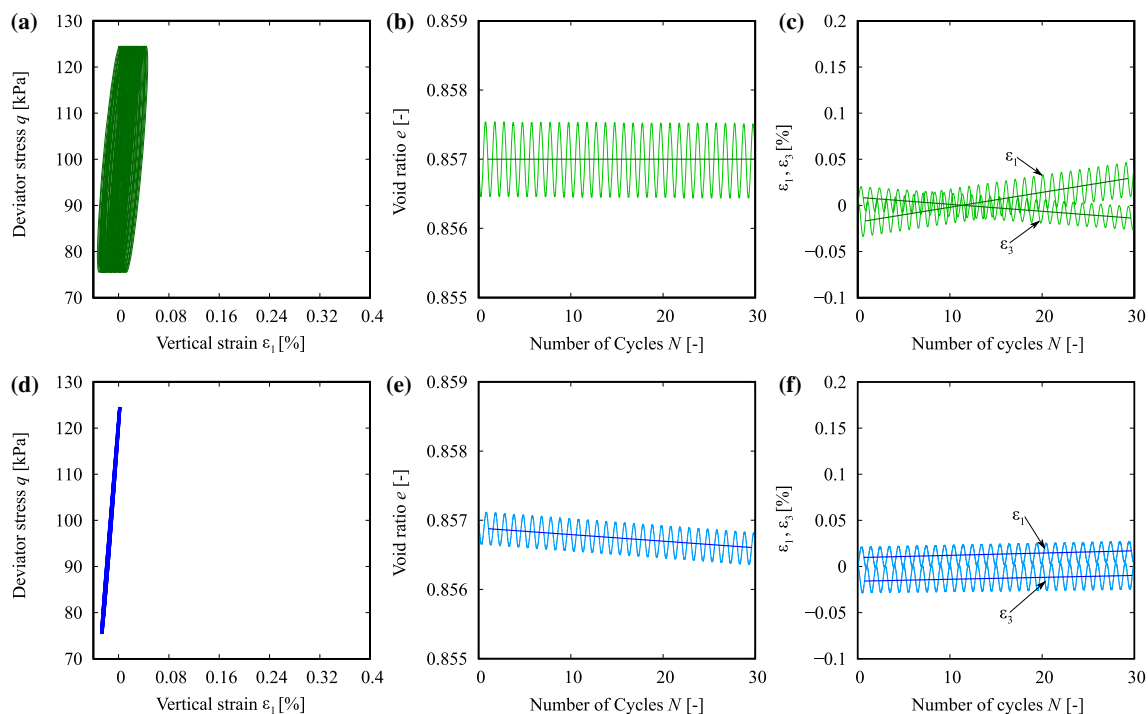


Fig. 10 Simulations with the (hypo-)“elastic” tensor of: (a–c) DM04/SANISAND-MSf models; (d–f) hypoelectric models

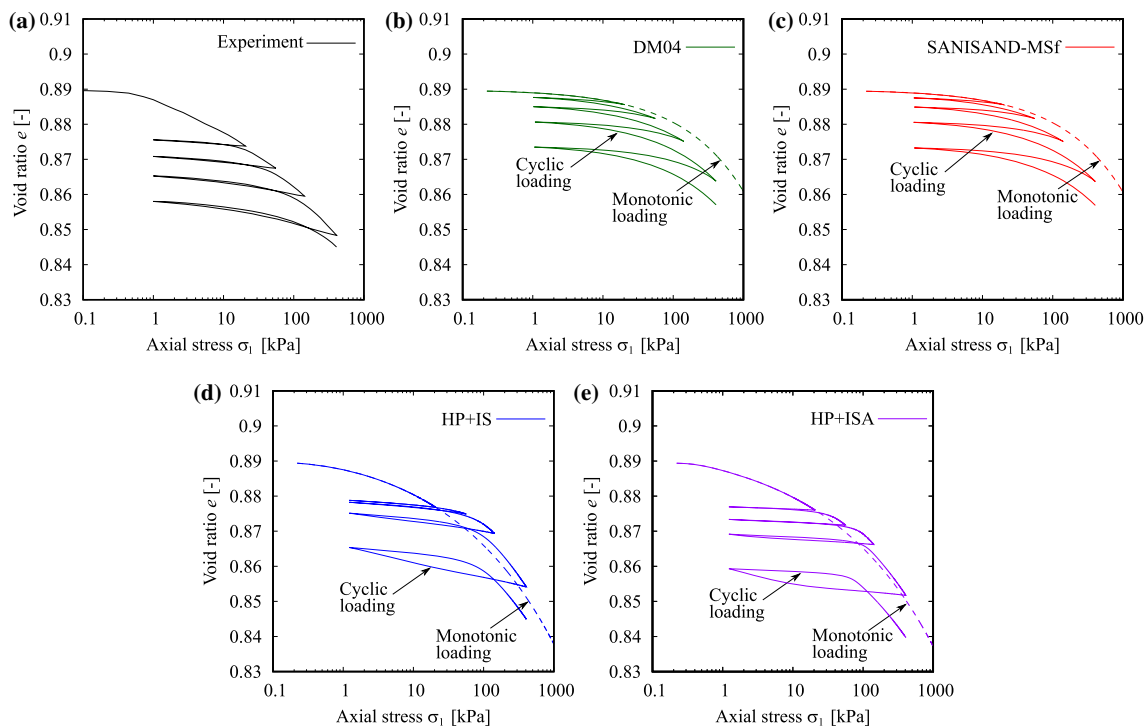


Fig. 11 Oedometric test with multiple unloading–reloading cycles: (a) Experiment on Karlsruhe fine sand reported by Wichtmann and Triantafyllidis [74]; and the corresponding simulations using (b) DM04; (c) SANISAND-MSf; (d) HP+IS; (e) HP+ISA

relevance. Although a cyclic oedometer test is considered to be simple, yet important, many deficiencies have been seen on their simulations. Problems concerning to the resulting oedometric stiffness, and overshooting/subshooting effects are characteristic drawbacks on these simulations. For illustration and analysis purposes, the cyclic oedometer reported by Wichtmann and Triantafyllidis [74] on Karlsruhe fine sand is used and shown in Fig. 11. The following initial conditions are thereby given: $e_0 = 0.8894$, $D_r = 44\%$, $\sigma_1 = 0.221$ kPa. It includes multiple unloading–reloading cycles with the following description: loading/reloading paths increases the axial stress to: (a) $\sigma_1 = 20.53$ kPa, (b) $\sigma_1 = 55.72$ kPa, (c) $\sigma_1 = 142.14$ kPa, (d) $\sigma_1 = 407.1$ kPa and (e) $\sigma_1 = 407.1$ kPa, respectively. All unloading paths reach always $\sigma_1 = 1$ kPa.

Simulations with the four models for cyclic loading are also included in Fig. 11, and their lack of congruence is evident: to start with, the DM04 and SANISAND-MSf models showed in general a stiffer behavior. This is because of the basic formulation of these models with an open ended narrow cone-type yield surface, hence not generating any plasticity under constant stress ratio loading. The main logic behind this assumption is that in sands, due to their granular nature, the predominant mechanism of plastic deformation is due to a change in stress ratio. The appropriateness of various choices of yield surface shape for sand and clay elastoplasticity models was discussed in

Taiebat and Dafalias [63]. In particular, it was proposed that yield surface for sands must be narrow with a shape that is more or less along a constant stress ratio line in the triaxial space, and for higher values of p' such shape must be closed, since high pressure can create plastic deformation by crushing of the sand grains. On that basis, Taiebat and Dafalias [62] proposed an additional mechanism in the SANISAND family for generating plastic strains under constant stress ratio loading, hence improving the model response in the related loading scenarios. The HP+IS and HP+ISA models perform better in regard to stiffness because they consider the void ratio characteristic loading curves, corresponding to the maximum, minimum, and critical state void ratios in their formulations. However, they simulate wrong in reloading paths: While overshooting is observed on the HP+IS model for all cases, undershooting is delivered by the HP+ISA model on larger strain amplitudes. Hence, it is shown that strain-based formulations, as the intergranular strain theory considered by the HP+IS and HP+ISA models, should be enhanced for correct assessment of memory effects where cycles with different strain amplitudes are reproduced. It is highly recommended to investigate how memory effects can be improved on IS-type formulations. The major overshooting of monotonic paths can be eliminated by coupling the IS formulation with ASBS [3], as already discussed in Sect. 4.1. The brick model by Simpson [56] gives some

hints about using multiple internal variables related to different strain amplitudes.

4.7 Limitation 7: effect of drained preloading in undrained shearing

Drained preloading events have shown a strong influence on subsequent undrained shearing paths. This effect is of particular importance in many engineering problems, where “slow” loading cycles under drained conditions may eventually occur before any rapid loading. Many problems dealing with environmental loads (winds, waves, flooding, etc.) may experience this effect, considering the stochastic nature of their velocities. A triaxial test including a drained preloading stage before an undrained shearing gives to researchers some hints about the material response under these conditions. These tests have clearly shown a strong influence of the drained preloading on the undrained shearing path [10–13, 70], effect which is frequently disregarded on cyclic models.

For analysis purposes, three triaxial experiments performed on Karlsruhe fine sand by Wichtmann [70], two of them with drained preloading, are shown in Fig. 12a, b. They were performed as follows: (a) undrained triaxial test with no drained preloading. Its initial conditions are ($e_0 = 0.941$, $D_r = 30\%$, $p'_0 = 300$ kPa). The undrained shearing ends at an axial strain of $\varepsilon_1 = 30\%$. (b) Undrained triaxial test with isotropic ($q = 0$) drained preloading to $p' = 800$ kPa. The preloading path follows the points $A \rightarrow B \rightarrow A$ as shown in Fig. 12a. The initial conditions (before the drained preloading) are ($e_0 = 0.937$, $D_r = 31\%$, $p'_0 = 300$ kPa). A subsequent undrained triaxial test was performed till reaching $\varepsilon_1 = 30\%$. (c) Undrained triaxial test with drained triaxial preloading. Same as the last test, with the difference, that a drained triaxial test was used as the preloading path. The drained triaxial test follows the points $A \rightarrow C \rightarrow A$ shown in Fig. 12a. The initial conditions (before the drained preloading) are ($e_0 = 0.937$, $D_r = 31\%$, $p'_0 = 300$ kPa). Subsequently, an undrained shearing till $\varepsilon_1 = 30\%$ was performed.

The experimental results are presented in Fig. 12a, b and show a serious affection of the undrained response due to the drained preloading. This is attributed to both small strain effects and memory effects. Simulations show that the SANISAND-MSf and HP+IS are the only ones to capture partly well the influence of the drained preloading effect on the undrained shearing. The SANISAND-MSf model reproduces the influence of the deviatoric preloading due to the introduction of memory surface, whose evolution during the deviatoric preloading increases the stiffness of the model. On the other hand, the HP+IS reproduces this behavior due to the fact that the IS approach by

Niemunis and Herle [44] accounts for small strain effects depending on the angle formed by loading and unloading strain rate. The HP+ISA model did not simulate this effect, consistently with the fact that an undershooting is usually obtained on reloading paths of medium strain amplitudes. The DM04 model has a similar effect as the HP+ISA model, because its yield surface is narrow, and lacks of memory effects on cycles of larger amplitudes.

5 Closure

In this work, seven characteristic limitations of models for cyclic loading for sands are presented and discussed, from which suggestions are given to help further development of cyclic constitutive models. Components of some formulations which are responsible for these limitations, for example, yield surface, elastic stiffness, and plastic strain rate, among others, are mentioned for the sake of clarity, considering that these components may be shared by many existing models. In the analysis, two models from the bounding surface plasticity family and two models from the hypoplastic family were considered. Some of the exposed limitations are described in the following lines:

1. Overshooting (or undershooting) phenomenon after reverse loading/immediate reloading paths is a characteristic artificial drawback in model simulations of the cyclic loading of sands. To adequately address this issue, considering the memory effects of recent reverse loading history in the cyclic models is recommended.
2. Simulation of cyclic mobility with undrained cyclic triaxial tests of symmetric deviator stress amplitude ($q^{\min} = q^{\max}$) is in general accompanied with one-way ratcheting in strain accumulation. Two specific considerations can be incorporated to adequately resolve this issue. The first is to induce a degrading stiffness cycle by cycle so as to generate large shear strain in the liquefaction state. The other is to control the balance of the shear modulus in the compression and extension side.
3. To adequately model the cyclic liquefaction strength curves or $CSR-N_{ini}$ considering various criteria for reaching initial liquefaction is a challenge in majority of available constitutive models. To reach the criterion of r_u , the model needs to induce a large amount of contraction upon unloading after dilation. To properly capture the shear strain-based initial liquefaction, a mechanism for generating large shear strain in liquefaction state is necessary. To quantitatively simulate cyclic liquefaction strength curves, one needs to consider effects of CSR, relative densities, and initial confinement.

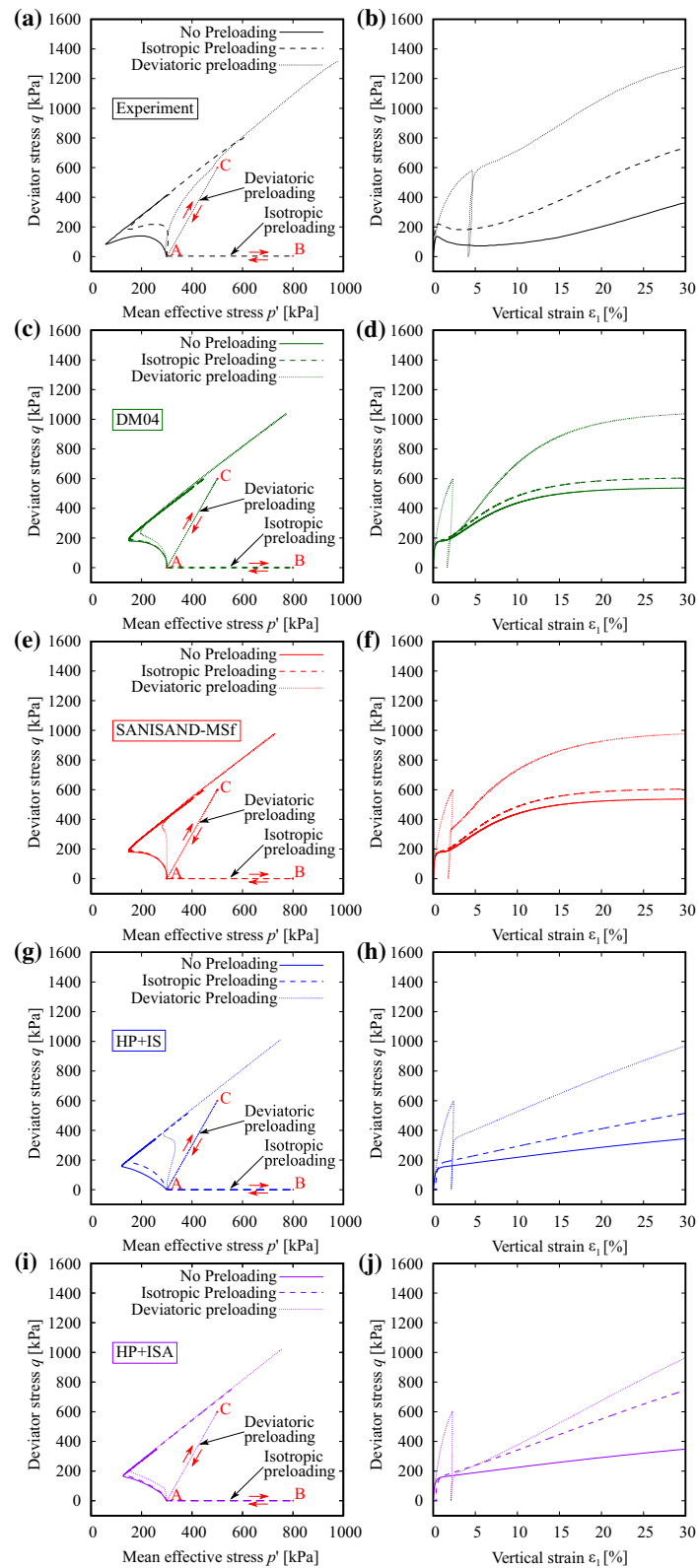


Fig. 12 Undrained monotonic triaxial tests with isotropic consolidation ($p'_0 = 300$ kPa) and different types of preloadings: (a, b) Experiments on Karlsruhe fine sand reported by Wichtmann [70]; and the corresponding simulations using (c, d) DM04; (e, f) SANISAND-MSf; (g, h) HP+IS; (i, j) HP+ISA

4. Simulation performance on very dense samples subjected to undrained cycles of constant large strain amplitudes also reveals some missing features in the constitutive models. A good amount of contraction should be generated upon unloading after dilation. The stress path attractor is accompanied by a degrading shear modulus.
5. The plastic strain accumulation is unrealistic when dealing with cyclic loading with closed stress loops of small amplitude, whereby much less accumulation of strains is expected. Attention should be given to the strain accumulation provided by the hypoelastic component of the models, to properly reduce the resulting strain accumulation.
6. The constitutive models when formulated only in terms of stress ratio changes for generating plasticity may deliver inadequate oedometric loading stiffness. Thus, in the formulation one may need to also account for plastic strains under constant stress ratio loading.
7. Drained preloading affects significantly the subsequent undrained shearing. This effect should not be neglected by constitutive models. Inadequate memory effects in the formulation of some models hinder the reproduction of this important aspect in modeling the subsequent undrained shearing.

Appendix

Notation and variables

The notation and convention is as follows: scalar magnitudes (e.g., *a*, *b*) are denoted by italic fonts, vectors (e.g., **a**, **b**) with bold lowercase fonts, second-rank tensors (e.g., **A**, **B**) with bold capital letter or bold symbols, higher

ranked tensors with special fonts (e.g., **E**, **L**). Components of these tensors are denoted through indicial notation (e.g., *A_{ij}*). δ_{ij} is the Kronecker delta, also represented with ($1_{ij} = \delta_{ij}$). The unit fourth-rank tensor for symmetric tensors is denoted by **I**, where $1_{ijkl} = \frac{1}{2}(\delta_{ik}\delta_{jl} + \delta_{il}\delta_{jk})$. The following operations hold: $\mathbf{A} : \mathbf{B} = A_{ij}B_{ij}$, $\mathbf{A} \otimes \mathbf{B} = A_{ij}B_{kl}$, $\|\mathbf{A}\| = \sqrt{A_{ij}A_{ij}}$, $\overline{\square} = \frac{\square}{\|\square\|}$, $\mathbf{A}^{\text{dev}} = \mathbf{A} - \frac{1}{3}(\text{tr}\mathbf{A})\mathbf{1}$, $\hat{\mathbf{A}} = \frac{\mathbf{A}}{\text{tr}(\mathbf{A})}$. Components of the effective stress tensor $\boldsymbol{\sigma}$ or strain tensor $\boldsymbol{\varepsilon}$ in compression are negative. Roscoe variables are defined as $p' = -\sigma_{ii}/3$, $q = \sqrt{\frac{3}{2}}\|\boldsymbol{\sigma}^{\text{dev}}\|$, $\varepsilon_v = -\varepsilon_{ii}$ and $\varepsilon_s = \sqrt{\frac{2}{3}}\|\boldsymbol{\varepsilon}^{\text{dev}}\|$. The stress ratio η is defined as $\eta = q/p'$.

Summary of constitutive equations for models for cyclic loading

Table 5 provides a summary of the constitutive equations of the DM04 model by Dafalias and Manzari [7] and the SANISAND-MSf model by Yang et al. [78]. A detailed guide for the calibration of the DM04 and SANISAND-MSf parameters can be found in Dafalias and Manzari [7], Taiebat and Dafalias [62] and Yang et al. [78].

The constitutive equations of the hypoplastic model for sands by Von Wolffersdorff [75] and the two different intergranular strain approaches by Niemunis and Herle [44] and Fuentes et al. [22] are presented in Table 6. A detailed guide for the calibration of the hypoplastic and conventional intergranular strain parameters can be found in Herle and Gudehus [26] and Niemunis and Herle [44], respectively. On the other hand, a guide for the calibration of the ISA-hypoplasticity parameters can be found in Fuentes [17] and Fuentes et al. [22].

Table 5 Constitutive relations of the elastoplastic models

Bounding surface plasticity model by Dafalias and Manzari [7]

$de_v^e = dp'/K$; $de^e = ds/(2G)$	$de_v^p = \langle L \rangle D$; $de^p = \langle L \rangle \mathbf{R}'$
$G = G_0 p_{at} (2.97 - e)^2 / (1 + e) (p'/p_{at})^{1/2}$	$K = 2(1 + \nu) / [3(1 - 2\nu)G]$
$f = \sqrt{(\mathbf{s} - p'\boldsymbol{\alpha}) : (\mathbf{s} - p'\boldsymbol{\alpha})} - \sqrt{2/3}pm$	$D = A_0(1 + \langle \mathbf{z} : \mathbf{n} \rangle)(\boldsymbol{\alpha}_\theta^b - \boldsymbol{\alpha}) : \mathbf{n}$
$\mathbf{R}' = B\mathbf{n} - C[\mathbf{n}^2 - (1/3)\mathbf{1}]$	$\mathbf{n} = (\mathbf{r} - \boldsymbol{\alpha}) / \ \mathbf{r} - \boldsymbol{\alpha}\ $
$B = 1 + 3(1 - c)/(2c)g(\theta, c) \cos 3\theta$	$C = 3\sqrt{3/2}(1 - c)g(\theta, c)/c$
$g(\theta, c) = 2c / [(1 + c) - (1 - c)\cos 3\theta]$	$d\boldsymbol{\alpha} = \langle L \rangle (2/3)h(\boldsymbol{\alpha}_\theta^b - \boldsymbol{\alpha})$
$d\mathbf{z} = -c_z \langle -de_v^p \rangle (-z_{\max}\mathbf{n} + \mathbf{z})$	$h = b_0 / [(\boldsymbol{\alpha} - \boldsymbol{\alpha}_{in}) : \mathbf{n}]$
$b_0 = G_0 h_0 (1 - c_h e) (p'/p_{at})^{-1/2}$	$\boldsymbol{\alpha}_\theta^d = \sqrt{2/3}[g(\theta, c)M \exp(n^d \psi) - m]\mathbf{n}$
$\boldsymbol{\alpha}_\theta^b = \sqrt{2/3}[g(\theta, c)M \exp(-n^b \psi) - m]\mathbf{n}$	$e_c = e_c^{\text{ref}} - \lambda_c (p'/p_{at})^\xi$

Table 5 continued

SANISAND-MSf model by Yang et al. [78]

$\mathbf{de}^p = \langle L \rangle \mathbf{R}^* ; \mathbf{R}^* = x_2^2 \mathbf{n} + (1 - x_2^2) \mathbf{R}' / \ \mathbf{R}'\ $	$x_x = \langle \alpha_{\theta_x}^b - \ \alpha\ \rangle / \alpha_{\theta_x}^b$
$\alpha_{\theta_x}^b = \sqrt{2/3} [g(\theta_x, c) M \exp(-n^b \psi) - m]$	$\cos 3\theta_x = \sqrt{6} \text{tr}(\mathbf{n}_x^2); \mathbf{n}_x = \alpha / \ \alpha\ $
$D = A_0 g(\theta, c)^{-n_s} (1 + \langle \mathbf{z} : \mathbf{n} \rangle) (\alpha_{\theta}^d - \alpha) : \mathbf{n}$	$b_0 = G_0 h_0 g(\theta, c)^{-n_s} (1 - c_h e) (p'/p_{at})^{-1/2}$
$f^M = \sqrt{(\alpha_{\theta}^M - \alpha^M) : (\alpha_{\theta}^M - \alpha^M)} - \sqrt{2/3} m^M$	$\alpha_{\theta}^M = \alpha^M + \sqrt{2/3} m^M \mathbf{n}$
$d\alpha^M = \langle L \rangle (2/3) h^M (\alpha_{\theta}^b - \alpha_{\theta}^M)$	
$dm^M = \langle L \rangle [\sqrt{2/3} c_c h^M (\alpha_{\theta}^b - \alpha_{\theta}^M) : \mathbf{n}] - m^M / \zeta (\alpha_{\theta}^b - \alpha_{\theta}^M) : \mathbf{n} \langle -D \rangle$	
$h^M = \{h + \sqrt{3/2} (m^M / \zeta) \text{sgn}[(\alpha_{\theta}^b - \alpha_{\theta}^M) : \mathbf{n}] \langle -D \rangle\} / (1 + c_c \mathcal{H}[(\alpha_{\theta}^b - \alpha_{\theta}^M) : \mathbf{n}])$	
$h = \{b_0 / [(\alpha - \alpha_{in}) : \mathbf{n}]\} \exp[\{\mu_0 / (\ \alpha_{in}\ ^u + \varepsilon)\} (b^M / b_{ref})^w]$	$b^M = (\alpha_{\theta}^M - \alpha) : \mathbf{n}; b_{ref} = (\alpha_{\theta}^b - \alpha_{\theta+\pi}^b)$
$d\ell = \langle L \rangle [c_\ell (1 - p_r) (1 - \ell)^{n_\ell}] - c_r \ell d\varepsilon_v $	$p_r = p' / p_{th}$
$h_0 = h'_0 [(1 - \langle 1 - p_r \rangle)^{x_\ell} + f_\ell]$	$A_0 = A'_0 [(1 - \langle 1 - p_r \rangle)^{x_\ell} + f_\ell]$

Table 6 Constitutive relations of the hypoplastic models

Hypoplastic model for sands by Von Wolffersdorff [75]

$\dot{\sigma} = \mathbf{M} : \dot{\varepsilon}$	$\mathbf{N}^{hyp} = f_d f_b f_e \frac{F a}{\hat{\sigma} : \hat{\sigma}} (\hat{\sigma} + \hat{\sigma}^{dev})$
$L^{hyp} = f_b f_e \frac{1}{\hat{\sigma} : \hat{\sigma}} (F^2 I + a^2 \hat{\sigma} \hat{\sigma})$	$f_e = \left(\frac{e_c}{e}\right)^\beta$
$f_b = \frac{h_s}{n} \left(\frac{1 + e_i}{e_i}\right) \left(\frac{e_{i0}}{e_{c0}}\right)^\beta \left(-\frac{\text{tr}\sigma}{h_s}\right)^{1-n} \left[3 + a^2 - \sqrt{3} a \left(\frac{e_{i0} - e_{d0}}{e_{c0} - e_{d0}}\right)^\alpha\right]^{-1}$	$f_d = \left(\frac{e - e_d}{e_c - e_d}\right)^\alpha$
$F = \sqrt{\frac{1}{8} \tan^2(\psi) + \frac{2 - \tan^2(\psi)}{2 + 2\sqrt{2} \tan(\psi) \cos(3\theta)}} - \frac{1}{2\sqrt{2} \tan(\psi)}$	$a = \frac{\sqrt{3}(3 - \sin(\varphi_c))}{2\sqrt{2} \sin(\varphi_c)}$
$e_c = e_{c0} \exp(-(3p'/h_s)^n)$	$e_i = e_{i0} \exp(-(3p'/h_s)^n)$
$e_d = e_{d0} \exp(-(3p'/h_s)^n)$	$\tan \psi = \sqrt{3} \ \hat{\sigma}^{dev}\ $
$\cos(3\theta) = \sqrt{6} \frac{\text{tr}(\hat{\sigma}^{dev} \hat{\sigma}^{dev} \hat{\sigma}^{dev})}{(\hat{\sigma}^{dev} : \hat{\sigma}^{dev})^{3/2}}$	

Intergranular Strain model by Niemunis and Herle [44]

$\mathbf{M} = m_1 \mathbf{L}^{hyp} + m_2 \mathbf{L}^{hyp} : \vec{\mathbf{h}} \vec{\mathbf{h}} + \rho^\lambda \mathbf{N}^{hyp} \vec{\mathbf{h}} \text{ for } \vec{\mathbf{h}} : \dot{\varepsilon} > 0$	$\dot{\mathbf{h}} = (1 - \vec{\mathbf{h}} \vec{\mathbf{h}} \rho^{\beta_r}) : \dot{\varepsilon} \text{ for } \vec{\mathbf{h}} : \dot{\varepsilon} > 0$
$\mathbf{M} = m_1 \mathbf{L}^{hyp} + m_3 \mathbf{L}^{hyp} : \vec{\mathbf{h}} \vec{\mathbf{h}} \text{ for } \vec{\mathbf{h}} : \dot{\varepsilon} \leq 0$	$\dot{\mathbf{h}} = \dot{\varepsilon} \text{ for } \vec{\mathbf{h}} : \dot{\varepsilon} \leq 0$
$m_1 = \rho^\lambda m_T + (1 - \rho^\lambda) m_R$	$m_2 = \rho^\lambda (1 - m_T)$
$m_3 = \rho^\lambda (m_R - m_T)$	$\rho = \ \mathbf{h}\ / R$

ISA-hypoplasticity by Fuentes et al. [22]

$\mathbf{M} = m(\mathbf{L}^{hyp} + \rho^\lambda \mathbf{N}^{hyp} \mathbf{N}) \text{ for } F_H = 0$	$F_H = \ \mathbf{h} - \mathbf{c}\ - R/2$
$\mathbf{M} = m_R \mathbf{L}^{hyp} \text{ for } F_H < 0$	$\mathbf{N} = (\mathbf{h} - \mathbf{c})^\rightarrow$
$m = m_R + (1 - m_R) y_h$	$\lambda_H = \frac{\langle \mathbf{N} : \dot{\varepsilon} \rangle}{1 + \mathbf{N} : \bar{\mathbf{c}}}$
$\dot{\mathbf{h}} = \dot{\varepsilon} - \lambda_H \mathbf{N}$	$\dot{\mathbf{c}} = \lambda_H \bar{\mathbf{c}}$
$\mathbf{c}_b = (R/2) \vec{\hat{\varepsilon}}$	$\mathbf{h}_b = R \mathbf{N}$
$y_h = \rho^\lambda \langle \mathbf{N} : \dot{\varepsilon} \rangle$	$\rho = 1 - \frac{\ \mathbf{d}_b\ }{2R}$

Table 6 (continued)

ISA-hypoplasticity by Fuentes et al. [22]

$$\mathbf{d}_b = \mathbf{h}_b - \mathbf{h}$$

$$\chi = \chi_0 + \varepsilon_{\text{acc}}(\chi_{\text{max}} - \chi_0)$$

$$\beta_h = \beta_{\text{hmax}} + (\beta_{h0} - \beta_{\text{hmax}})(1 - f_z)f_h$$

$$f_h = |\vec{\mathbf{e}} : \vec{\mathbf{d}}_b|$$

$$f_e = f_{e0} - f_z(f_{e0} - 1)$$

$$f_d = f_{d0} + f_z(1 - f_{d0})$$

$$F_d = \frac{q/p'}{M_c F f_{d0}}$$

$$\bar{\mathbf{c}} = \beta_h(\mathbf{c}_b - \mathbf{c})/R$$

$$\dot{\varepsilon}_{\text{acc}} = \frac{c_a}{R}(1 - y_h - \varepsilon_{\text{acc}}) \|\dot{\varepsilon}\|$$

$$\dot{\mathbf{Z}} = c_z \langle F_d \rangle (\mathbf{N} - \mathbf{Z}) \|\dot{\varepsilon}\|$$

$$\vec{\mathbf{d}}_b = (R \vec{\mathbf{e}} - \mathbf{h})^{-}$$

$$f_{e0} = \left(\frac{e_c}{e}\right)^\beta$$

$$f_{d0} = \left(\frac{e - e_d}{e_c - e_d}\right)^\alpha$$

$$f_z = \langle -\mathbf{Z} : \mathbf{N} \rangle$$

Acknowledgements Jose Duque and David Mašín appreciate the financial support given by the Center for Geosphere Dynamics (UNCE/SCI/006) and by the INTER-EXCELLENCE project LTACH19028 by the Czech Ministry of Education, Youth and Sports. Jose Duque acknowledges the financial support given by the Charles University Grant Agency (GAUK) with project number 200120. Ming Yang and Mahdi Taiebat acknowledge the support from the Natural Sciences and Engineering Research Council of Canada (NSERC). Yannis F. Dafalias's help in reviewing the parts related to the plasticity models is acknowledged.

References

- Armstrong R (2018) Numerical analysis of leap centrifuge tests using a practice-based approach. *Soil Dyn Earthq Eng* 113:793–803
- Barrero A, Taiebat M, Dafalias Y (2020) Modeling cyclic shearing of sands in the semifluidized state. *Int J Num Anal Methods Geomech* 44(3):371–388
- Bode M, Fellin W, Medicus G (2021) Reloading in barodesy employing the asymptotic state boundary surface. *Int J Num Anal Methods Geomech*. <https://doi.org/10.1002/nag.3258>
- Boulanger RW, Ziotopoulou K (2013) Formulation of a sand plasticity plane-strain model for earthquake engineering applications. *Soil Dyn Earthq Eng* 53:254–267
- Cudny M, Truty A (2020) Refinement of the hardening soil model within the small strain range. *Acta Geotechnica* 15:2031–2051
- Dafalias Y (1986) An anisotropic critical state soil plasticity model. *Mech Res Commun* 13(6):341–347
- Dafalias Y, Manzari M (2004) Simple plasticity sand model accounting for fabric change effects. *J Eng Mech* 130(6):634–662
- Dafalias Y, Taiebat M (2016) SANISAND-Z: zero elastic range sand plasticity model. *Géotechnique* 66(12):999–1013
- Darby K, Hernandez G, DeJong J, Boulanger R (2019) Centrifuge model testing of liquefaction mitigation via microbially induced calcite precipitation. *J Geotech Geoenviron Eng* 145(10):04019084
- Doanh T, Dubujet P, Touron G (2010) Exploring the undrained induced anisotropy of Hostun rf loose sand. *Acta Geotechnica* 5(4):239–256
- Doanh T, Finge Z, Boucq S, Dubujet P (2006) Histotropy of Hostun RF loose sand. In: *Modern Trends in Geomechanics*, pp. 399–411
- Doanh T, Ibraim E, Matiotti R (1997) Undrained instability of very loose Hostun sand in triaxial compression and extension. Part 1: experimental observations. *Mech Cohes Frict Mater* 2(1):47–70
- Dubujet P, Doanh T (1997) Undrained instability of very loose Hostun sand in triaxial compression and extension. part 2: theoretical analysis using an elastoplasticity model. *Mech Cohes Frict Mater* 2(1):71–92
- Duque J, Mašín D, Fuentes W (2020) Improvement to the intergranular strain model for larger numbers of repetitive cycles. *Acta Geotechnica* 15:3593–3604
- Elgamal A, Yang Z, Parra E (2002) Computational modeling of cyclic mobility and post-liquefaction site response. *Soil Dyn Earthq Eng* 22(4):259–271
- Elgamal A, Yang Z, Parra E, Ragheb A (2003) Modeling of cyclic mobility in saturated cohesionless soils. *Int J Plast* 19(6):883–905
- Fuentes W (2014) Contributions in mechanical modelling of fill materials. Karlsruhe Institute of Technology, Germany (**PhD thesis**)
- Fuentes W, Mašín D, Duque J (2021) Constitutive model for monotonic and cyclic loading on anisotropic clays. *Géotechnique* 71(8):657–673
- Fuentes W, Tafili M, Triantafyllidis T (2017) Constitutive model for clays under the isa framework. In: *Holistic simulation of geotechnical installation processes, benchmarks and simulations*, chapter 6, pages 115–129. Springer
- Fuentes W, Triantafyllidis T (2015) ISA model: a constitutive model for soils with yield surface in the intergranular strain space. *Int J Numer Anal Methods Geomech* 39(11):1235–1254
- Fuentes W, Triantafyllidis T, Lascarro C (2017) Evaluating the performance of an isa-hypoplasticity constitutive model on problems with repetitive loading. *Holistic simulation of geotechnical installation processes*. Springer, pp 341–362
- Fuentes W, Wichtmann T, Gil M, Lascarro C (2020) ISA-Hypoplasticity accounting for cyclic mobility effects for liquefaction analysis. *Acta Geotech* 15:1513–1531
- Ghoriaby M, Park H, Manzari M (2020) Physical and mechanical properties of ottawa f65 sand. In: *Model tests and numerical simulations of liquefaction and lateral spreading*. LEAP-UCD-2017, pp. 45–67
- Grabe P, Clayton C (2009) Effects of principal stress rotation on permanent deformation in rail track foundations. *J Geotech Geoenviron Eng* 135(4):555–565
- Gudehus G (2011) *Physical Soil Mechanics*. Springer, Berlin

26. Herle I, Gudehus G (1999) Determination of parameters of a hypoplastic constitutive model from properties of grain assemblies. *Mech Cohes Frict Mater* 4(5):461–486
27. Hyodo M, Hyde A, Aramaki N (1998) Liquefaction of crushable soils. *Géotechnique* 48(4):527–543
28. Iai S, Tobita T, Ozutsumi O, Ueda K (2011) Dilatancy of granular materials in a strain space multiple mechanism model. *Int J Numer Anal Methods Geomech* 35(3):360–392
29. Idriss I, Boulanger R (2008) Soil liquefaction during earthquakes. University of California, Davis (**Technical report**)
30. Idriss IM, Boulanger RW (2008) Soil liquefaction during earthquakes. Earthquake Engineering Research Institute, Oakland, CA. Monograph MNO-12, pp. 261
31. Inam A, Ishikawa T, Miura S (2012) Effect of principal stress axis rotation on cyclic plastic deformation characteristics of unsaturated base course material. *Soils Found* 52(3):465–480
32. Ishihara K (1993) Liquefaction and flow failure during earthquakes. *Géotechnique* 43(3):351–415
33. Ishihara K (1996) Soil behaviour in earthquake geotechnics. Oxford University Press, New York
34. Ishihara K, Yamazaki F (1980) Cyclic simple shear tests on saturated sand in multidirectional loading. *Soils Found* 20(1):45–59
35. Kan M, Taiebat H (2014) On implementation of bounding surface plasticity models with no overshooting effect in solving boundary value problems. *Comput Geotech* 55:103–116
36. Kumar S, Krishna A, Dey A (2020) Assessment of dynamic response of cohesionless soil using strain-controlled and stress-controlled cyclic triaxial tests. *Geotech Geol Eng* 38:1431–1450
37. Liao D, Yang Z (2021) Hypoplastic modeling of anisotropic sand behavior accounting for fabric evolution under monotonic and cyclic loading. *Acta Geotechnica*
38. Manzari M, Dafalias Y (1997) A critical state two-surface plasticity model for sands. *Géotechnique* 47(2):255–272
39. Marshall S, Park T (1976) Liquefaction potential evaluated from cyclic strain-controlled properties tests on sands. *Soils Found* 16(3):51–65
40. Matsuda H, Hendrawan A, Ishikura R, Kawahara S (2011) Effective stress change and post-earthquake settlement properties of granular materials subjected to multi-directional cyclic simple shear. *Soils Found* 51(5):873–884
41. Ng W, Sun H, Lei G, Shi J, Mašín D (2015) Ability of three different soil constitutive models to predict a tunnel's response to basement excavation. *Can Geotech J* 52(11):1685–1698
42. Niemunis A (2003) Extended Hypoplastic Models for Soils. Institute for Foundation Engineering and Soil Mechanics, Ruhr-University Bochum, Germany, Habilitation
43. Niemunis A, Cudny M (2018) Poor performance of the HSS model: discussion on dynamic soil-structure interaction: a three-dimensional numerical approach and its application to the lotung case study. *Comput Geotech*
44. Niemunis A, Herle I (1997) Hypoplastic model for cohesionless soils with elastic strain range. *Mech Cohes Frict Mater* 2(4):279–299
45. Papadimitriou A, Bouckovalas G (2002) Plasticity model for sand under small and large cyclic strains: a multiaxial formulation. *Soil Dyn Earthq Eng* 22(3):191–204
46. Poblete M, Fuentes W, Triantafyllidis T (2016) On the simulation of multidimensional cyclic loading with intergranular strain. *Acta Geotechnica* 11(6):1263–1285
47. Porcino D, Marciano V, Ghionna V (2009) Influence of cyclic pre-shearing on undrained behaviour of carbonate sand in simple shear tests. *Geomech Geoenviron* 4(2):151–161
48. Prada L (2011) Praelastic description of small-strain behaviour. Karlsruhe Institute of Technology, Germany (**PhD thesis**)
49. Pradhan T, Tatsuoka F (1989) On stress-dilatancy equations of sand subjected to cyclic loading. *Soils Found* 29(1):65–81
50. Pradhan T, Tatsuoka F, Mohri Y, Sato Y (1989) An automated triaxial testing system using a simple triaxial cell for soils. *Soils Found* 29(1):151–160
51. Pradhan T, Tatsuoka F, Sato Y (1989) Experimental stress-dilatancy relations of sand subjected to cyclic loading. *Soils Found* 29(1):45–64
52. Prevost J (1985) A simple plasticity theory for frictional cohesionless soils. *Soil Dyn Earthq Eng* 4(1):9–17
53. Pyke R, Seed H, Chan C (1975) Settlement of sands under multidirectional shaking. *J Geotech Eng Div* 101(4):379–398
54. Rayamajhi D (2014) Shear reinforcement effects of discrete columns in liquefiable soils. Oregon State University, PhD thesis
55. Seed B, Martin G, Pyke R (1978) Effect of multidirectional shaking on pore pressure development in sands. *J Geotech Eng Div* 104(1):27–44
56. Simpson B (1992) Retaining structures: displacement and design, 32nd rankine lecture. *Géotechnique* 42(4):541–576
57. Sivathayalan S (1994) Static, cyclic and post liquefaction simple shear response of sands. The University of British Columbia (Master Thesis)
58. Sivathayalan S, Logeswaran P, Manmatharajan V (2015) Cyclic resistance of a loose sand subjected to rotation of principal stresses. *J Geotech Geoenviron Eng* 141(3):04014113
59. Sriskandakumar S (2004) Cyclic loading response of fraser river sand for validation of numerical models simulating centrifuge tests. The University of British Columbia (Master Thesis)
60. Su D, Li X (2008) Impact of multidirectional shaking on liquefaction potential of level sand deposits. *Géotechnique* 58(4):259–267
61. Taiebat M (2008) Advanced Elastic-Plastic Constitutive and Numerical Modeling in Geomechanics. University of California, Davis (**PhD thesis**)
62. Taiebat M, Dafalias Y (2008) SANISAND, simple anisotropic sand plasticity model. *Int J Num Anal Methods Geomech* 32(8):915–948
63. Taiebat M, Dafalias Y (2010) Simple yield surface expressions appropriate for soil plasticity. *Int J Geomech* 10(4):161–169
64. Taiebat M, Jeremić B, Dafalias YF, Kaynia AM, Cheng Z (2010) Propagation of seismic waves through liquefied soils. *Soil Dyn Earthq Eng* 30(4):236–257
65. Tatsuoka F, Ishihara K (1974) Drained deformation of sand under cyclic stresses reversing direction. *Soils Found* 14(3):51–65
66. Vasko A (2015) An investigation into the behavior of ottawa sand through monotonic and cyclic shear tests. George Washington University (Master Thesis)
67. Vaucetic M, Mortezaie A (2015) Cyclic secant shear modulus versus pore water pressure in sands at small cyclic strains. *Soil Dyn Earthq Eng* 70:60–72
68. Wang G, Xie Y (2014) Modified bounding surface hypoplasticity model for sands under cyclic loading. *J Geotech Geoenviron Eng* 140(1):91–101
69. Wang Z, Dafalias Y, Shen C (1990) Bounding surface hypoplasticity model for sand. *J Eng Mech* 116(5):983–1001
70. Wichtmann T (2016) Soil behaviour under cyclic loading: experimental observations, constitutive description and applications. Habilitation, Karlsruhe Institute of Technology (KIT)
71. Wichtmann T, Fuentes W, Triantafyllidis T (2019) Inspection of three sophisticated constitutive models based on monotonic and cyclic tests on fine sand: hypoplasticity vs. Sanisand vs. ISA. *Soil Dyn Earthq Eng* 124:172–183
72. Wichtmann T, Niemunis A, Triantafyllidis T (2007) On the influence of the polarization and the shape of the strain loop on strain accumulation in sand under high-cyclic loading. *Soil Dyn Earthq Eng* 27(1):14–28

73. Wichtmann T, Triantafyllidis T (2016) An experimental data base for the development, calibration and verification of constitutive models for sand with focus to cyclic loading. part I: tests with monotonic loading and stress cycles. *Acta Geotechnica* 11(4):739–761
74. Wichtmann T, Triantafyllidis T (2016) An experimental data base for the development, calibration and verification of constitutive models for sand with focus to cyclic loading. part II: tests with strain cycles and combined loading. *Acta Geotechnica* 11(4):763–774
75. Wolffersdorff V (1996) A hypoplastic relation for granular materials with a predefined limit state surface. *Mech Cohes Frict Mater* 1(3):251–271
76. Wu W, Bauer E (1994) A simple hypoplastic constitutive model for sand. *Int J Num Anal Methods Geomech* 18(12):833–862
77. Yamada Y, Ishihara K (1983) Undrained deformation characteristics of sand in multidirectional shear. *Soils Found* 23(1):61–79
78. Yang M, Taiebat M, Dafalias Y (2020) SANISAND-MSf: a memory surface and semifluidized state enhanced sand plasticity model for undrained cyclic shearing. *Géotechnique*. <https://doi.org/10.1680/jgeot.19.P.363>
79. Yang Z, Elgamal A, Parra E (2003) Computational model for cyclic mobility and associated shear deformation. *J Geotech Geoenviron Eng* 129(12):1119–1127
80. Zhang J, Wang G (2012) Large post-liquefaction deformation of sand, part I: physical mechanism, constitutive description and numerical algorithm. *Acta Geotechnica* 7(2):69–113

Publisher's Note Springer Nature remains neutral with regard to jurisdictional claims in published maps and institutional affiliations.